

Submitted to *The Astrophysical Journal*

Three-Dimensional Simulations of Jets from Keplerian Disks: Self-Regulatory Stability

RACHID OUYED

*Nordic Institute for Theoretical Physics, Blegdamsvej 17 DK-2100 Copenhagen Ø,
Denmark.*

ouyed@nordita.dk

DAVID A. CLARKE¹

*Department of Astronomy and Physics, Institute for Computational Astrophysics, Saint
Mary's University, Halifax, Nova Scotia B3H 3C3, Canada*

dclarke@ap.stmarys.ca

and

RALPH E. PUDRITZ²

*Department of Physics and Astronomy, McMaster University, Hamilton, Ontario
L8S 4M1, Canada*

pudritz@mcmaster.ca

ABSTRACT

We present the extension of previous two-dimensional simulations of the time-dependent evolution of non-relativistic outflows from the surface of Keplerian accretion disks, to three dimensions. As in the previous work, we investigate the outflow that arises from a magnetised accretion disk, that is initially in hydrostatic balance with its surrounding cold corona. The accretion disk itself is taken to provide a set of fixed boundary conditions for the problem.

¹on sabbatical leave at l'Observatoire de Grenoble BP53 – F-38041, Grenoble Cedex 9, France

²on sabbatical leave at TAPIR, Caltech, 130-33, Pasadena, CA 91125, USA

We find that the mechanism of jet acceleration is identical to what was established from the previous 2-D simulations. The 3-D results are consistent with the theory of steady, axisymmetric, centrifugally driven disk winds up to the Alfvén surface of the outflow. Beyond the Alfvén surface however, the jet in 3-D becomes unstable to non-axisymmetric, Kelvin-Helmholtz instabilities. The most important result of our work is that while the jet is unstable at super-Alfvénic speeds, it survives the onset of unstable modes that appear in this physical regime.

We show that jets maintain their long-term stability through a self-limiting process wherein the average Alfvénic Mach number within the jet is maintained to order unity. This is accomplished in at least two ways. First, poloidal magnetic field is concentrated along the central axis of the jet forming a “backbone” in which the Alfvén speed is sufficiently high to reduce the average jet Alfvénic Mach number to unity. Second, the onset of higher order Kelvin-Helmholtz “flute” modes ($m \geq 2$) reduce the efficiency with which the jet material is accelerated, and transfer kinetic energy of the outflow into the stretched, poloidal field lines of the distorted jet. This too has the effect of increasing the Alfvén speed, and thus reducing the Alfvénic Mach number. The jet is able to survive the onset of the more destructive $m = 1$ mode in this way.

Our simulations also show that jets can acquire corkscrew, or wobbling types of geometries in this relatively stable end-state, depending on the nature of the perturbations upon them. Finally, we suggest that jets go into alternating periods of low and high activity as the disappearance of unstable modes in the sub-Alfvénic regime enables another cycle of acceleration to super-Alfvénic speeds.

Subject headings: Winds: accretion, accretion disks- proto-stars: jets-ISM: jets and outflows-MHD: magnetic fields

1. INTRODUCTION

Astrophysical jets are observed to be associated with young stellar objects (e.g. reviews by Königl & Pudritz, 2000), as well as stellar-mass (Mirabel & Rodríguez 1998) and super-massive black holes (Begelman, Blandford & Rees 1984). Most, if not all, of the jets in this diverse collection are observed to have accretion disks associated with their central objects. Observations of jets from young stellar objects (YSOs) reveal that the accretion rate through the underlying disk is proportional to the mass loss rate carried in the jet, suggestive of a direct physical link between them. Moreover, both the radiation fields and rotation rates of low mass YSOs are observed to be far too feeble to launch either radiatively, or magneto-

hydrodynamically (MHD) driven winds, again suggesting that the outflow originates on the disk. The MHD nature of jets in YSOs was supported by the discovery of strong magnetic fields associated with the jet from T-Tauri (Ray et al. 1997), as well as by the observed narrowing of the opening angle of such jets with increasing distance from the central object in spite of dwindling external gas pressure (Burrows et al. 1996).

Blandford & Payne (1982, henceforth BP) were the first to show that accretion disks, if threaded by large-scale, open magnetic field lines, will have their surface layers stripped away and flung out by the centrifugal stresses that act along such field lines. These outflows are subsequently collimated by the inescapable hoop-stress that arises from the toroidal magnetic field that develops within the jet itself. Jets in this picture are ultimately powered by the gravitational binding energy released during disk accretion. This simple, elegant picture of centrifugally accelerated disk winds potentially provides a universal model for jets in quasars (BP), microquasars (e.g., Mirabel & Rodriguez 1998) as well as YSOs (Pudritz & Norman 1983, 1986). Furthermore, it is unlikely that jets are merely exotic oddities in astrophysics. MHD jets probably play a fundamental role in the physics of star formation, as well as black hole building because they can be even more efficient in stripping out the angular momentum of gas in the accretion disk than MHD turbulence (e.g., Pelletier & Pudritz 1992).

Although the mechanism for the acceleration and collimation of MHD disk winds is conceptually clear, a detailed mathematical understanding of this phenomenon has proven to be elusive. Not much of a general quantitative nature is known beyond the predictions of conservation laws that pertain to time-dependent, axisymmetric, ideal MHD flows, or the predictions of models with additional simplifying assumptions (e.g., the imposition of self-similarity for time-independent, axisymmetric outflows, as in BP; Ostriker 1997; Ferreira 1997). In spite of the concerted efforts of a large number of theorists, the challenge of finding general solutions to the highly non-linear, “Grad-Shafranov” equations for MHD jets (which have three types of MHD wave propagation) has proven to be insurmountable (see Heinemann & Olbert 1978, for a general discussion). A more general and natural approach to finding both stationary as well as time-dependent solutions to the jet problem therefore, is through the use of time-dependent MHD simulations. The advent of MHD codes over the last decade is rapidly transforming our knowledge about this rich and complex problem.

Most of the simulations of MHD disk winds published to date are axisymmetric. The results of such simulations are in broad agreement with theoretical work on centrifugally driven outflows (e.g., Ouyed & Pudritz 1997a; 1997b; 1999, hereafter OPI, OPII, and OPIII; Romanova et al. 1997; Kudoh, Matsumoto, & Shibata 1998; Meier et al. 1997; Krasnopolsky, Li, & Blandford 2002, hereafter KLB). The collimation of jets by the “hoop stress” engendered by their toroidal fields has been observed in simulations that posit modest gradients of the

magnetic field across the underlying accretion disk (e.g., OPI; KLB). One caveat is that outflows produced by disks threaded by a steeply declining poloidal magnetic field, such as the extreme case of the split-monopole distribution of Romanova et al. (1997), do not appear to collimate well. Spruit, Foglizio & Stehle (1997) argue that jets from accretion disks should be strongly unstable to helical modes, and that jets, therefore, might be collimated by larger-scale poloidal magnetic fields rather than by magnetic hoop stress.

The purpose of the present paper is to investigate one of the principle remaining challenges in the theory of jets, namely, why are real 3-D jets so stable over great distances in spite of the fact that they are probably threaded by strong toroidal fields? It is well known that the purely toroidal field configurations that are used to help confine static, 3-D, Tokamak plasmas are unstable (e.g., Roberts 1967; Bateman 1980). The resulting kink, or helical ($m = 1$) mode instability derived from a 3-D linear stability analysis is powered by the free energy in the toroidal field, namely $B_\phi^2/8\pi$ (Eichler 1993). Shouldn't this instability affect the longevity of astrophysical jets too?

There are several major differences between the physics of astrophysical jets, and the simpler Tokamak configurations. First, jet plasmas are not static but consist of gas that typically has been accelerated to velocities greater than the fast magnetosonic (FM) wave (e.g., with an FM Mach number, M_{FM} , of several). A jet moving with sufficiently large FM Mach number, and which carries a current, can also suppress the growth of several types of instabilities. Second, astrophysical jets are threaded by a “backbone” of purely poloidal magnetic flux which may act to stiffen the jet against short-wavelength kink instabilities. One anticipates therefore that jets with poloidal fields at their core might still be unstable to wavelengths much longer than their width, but may very well survive such transverse motions. Finally, in previous simulations of 2-D jets (OPI), it was found that in the final, stationary jet, twice as much energy is carried by the bulk poloidal outflow (kinetic energy) than by the dominant toroidal magnetic field. This may also be a factor that favours the stability of jets, if it can be demonstrated to occur in 3-D outflows as well (see also KLB).

Analytic studies of the stability of 3-D, non-relativistic jets have focussed mainly on linear stability analysis of rather idealised jet configurations. These assume that jets have a radial, top-hat velocity profile, such as that of the pressure driven flow arising from an over-pressured orifice. The stability of 3-D jets of this type, which also contain purely poloidal or toroidal magnetic fields, is discussed by Ray (1981); Ferrari, Trussoni & Zaninetti (1981); Fiedler & Jones (1984), and many others. As an example, Ray (1981) showed that the growth rate of the Kelvin-Helmholtz (K-H) helical (kink) modes for all wavelengths longer than the jet radius R (i.e., $kR \leq 1$), vanish if flows are sub-Alfvénic.

The growth rates of helical modes in super-Alfvénic jets is lower than that of purely

hydrodynamic jets. More recent work by Appl & Camezind (1992) examined the stability of more general, current-carrying jets that contain force-free, helical magnetic fields. These latter systems are more stable than their purely hydrodynamic, or even purely poloidally magnetised, counterparts. These authors also found that jets are increasingly stabilised at progressively larger scales as the jet M_{FM} is increased.

Several extensive numerical simulations and studies of the stability of simple, 3-D, uniform jets may be found in the literature. For example, Hardee & Rosen (1999) performed 3-D simulations of “equilibrium” jets, and found that these uniform, magnetised jet models remain Kelvin-Helmoltz stable to low-order, surface helical and elliptical modes ($m = 1, 2$), provided that jets are on average sub-Alfvénic. This is in accord with the prediction of linear stability analysis. However, most configurations for jet simulations use rather *ad hoc* prescriptions for the initial toroidal field configuration (e.g., Todo et al. 1993; Lucek & Bell 1996; Hardee & Rosen 1999, to cite only a few) so that it is difficult to assess how pertinent the results are to the case of a jet that establishes its own toroidal field as the jet is accelerated from the accretion disk. In general, the available analytic and numerical results for the stability of simple jets show that the fastest growing modes are of K-H type. These K-H instabilities are increasingly stabilised for super-Alfvénic jets, as M_{FM} is increased much beyond unity. It is also generally known that sub-Alfvénic jets are stable. Taken together, these results suggest that 3-D jets are the most prone to K-H instabilities a bit beyond their Alfvén surface³, a region wherein their destabilising super-Alfvénic character cannot yet be offset by the stabilising effects engendered at large super FM numbers (e.g., Hardee & Rosen 1999). If this is so, then simulations should include the region not too far from the acceleration zone, beyond the putative Alfvén surface.

This paper presents a numerical investigation of the stability of 3-D MHD jets launched by accretion disks. The strategy is to extend to three dimensions previous work on the simulation of axisymmetric, time-dependent jets from Keplerian accretion disks (OPI, OPII, and OPIII). These 2-D simulations made use of the ZEUS-2D code of Stone & Norman (1992a, 1992b) and demonstrated the existence of stationary jets with properties that well match the predictions of the theoretical literature. They also revealed a class of new, intrinsically time-dependent episodic jets. It is natural therefore to extend our basic model approach, which rests on a secure numerical and physical foundation, to 3-D. Our basic finding is that 3-D jets, driven by an underlying disk for a particular magnetic configuration, are ultimately stable. The simulations show that there are mechanisms that help preserve the integrity of real astrophysical jets despite the growth of unstable modes within them.

³The Alfvén surface is defined by the set of Alfvén points where $M_A = 1$, (r_A, z_A) , of the flow along each jet field line.

We outline the physical model underlying all of our simulations in §2 and detail our numerical methods in §3. We show representative simulations from two classes of simulations in which the Kepler rotation of the disk (a boundary condition of the simulations) is either sharply or gradually truncated at the inner disk edge (sections §4 and §5 respectively). We then analyse our data and show that stabilisation of jets by non-linear saturation of K-H instabilities appears to be the basic mechanism. We conclude in §6.

2. BASIC PHYSICAL MODEL

In an earlier series of papers (OPI, OPII, and OPIII), the behaviour of time-dependent, non-relativistic disk winds in 2-D was investigated with the intent of studying their acceleration and collimation. To this end, a particularly simple, and analytically tractable model for an accretion disk and its surrounding corona was chosen with a common threading magnetic field. The key simplification in this approach is to examine the physics of the outflow for fixed physical conditions in the accretion disc (see also Romanova et al. 1997; Ustyugova et al. 1998). In part, this simplification may be justified by the fact that typically, accretion discs will evolve on longer time scales than their associated jets. We retain this approach in the present 3-D work.

Our physical model consists of an accretion disc whose surface pressure matches the pressure of an overlying, non-rotating corona in hydrostatic balance within an unsoftened gravitational potential well from a central object. As discussed in OPI, the resulting analytical model for the corona in scaled units is then given by:

$$\rho = \frac{1}{r^{1/\gamma-1}}; \quad \Phi = -\frac{1}{r} \quad (1)$$

where ρ is the matter density, Φ is the gravitational potential, r is the radial distance from the central object, and $\gamma = 5/3$ is the adiabatic index of the gas.

In OPI and OPII, the pressure was given by assuming a strict polytropic gas, with polytropic index equal to γ (thus, $p \sim \rho^\gamma$), and we follow this strategy here.⁴ Therefore, no

⁴This has the advantage of simplicity, particularly when trying to establish a numerically stable atmosphere using the gravitational potential. However, the disadvantages of using a strict polytrope include not being able to track contact discontinuities (e.g., between the disc and the corona) and not getting the Rankine-Hugoniot jump-conditions right (entropy is strictly conserved everywhere, including across shocks). Independent simulations performed by D.A.C. using the full energy equation show that these concerns have minimal impact on the simulations presented herein because much of the flow is subsonic. Qualitative differences between the polytropic and adiabatic equations of state appear only for supersonic flows where shocks and contact discontinuities play dynamically significant roles.

separate internal energy variable needs to be tracked.

A corona in hydrostatic balance is implemented numerically so that left unperturbed, it remains in perfect numerical balance indefinitely to within machine round-off errors. We note in passing that without due care, the atmosphere can be extremely unstable numerically, *particularly when the internal energy equation is used*. In particular, if numerical errors generated near the origin where the gradients are extremely steep are not specifically addressed, interpolation errors will cause pressure gradients near the origin to be consistently overestimated, thereby launching a thin, fast jet along the symmetry axis. These jets are completely numerical in origin, destroy the atmosphere through which they propagate before the physical outflow can be established, and at the very least, corrupt the results from the physical jets launched later by fully physical means. Additional details will be published in a future paper. In part, our use of the polytropic equation of state was to help squelch this very effect.

As discussed in OPI, the physical conditions on the rotation axis $r = 0$ of this model require special attention. The accretion disk will have an inner edge, either because it abuts the outer surface of a YSO, or because it is terminated by the magnetosphere of the central object. Any gas or objects interior to this inner disk edge are taken to be non-rotating. In this paper, we accomplish this in two different ways. First, as in OPI and OPII, we simply truncate the Keplerian velocity profile abruptly at the inner radius (simulations A–D). Second, in simulation E, we adopt a velocity structure on the inner disk edge that falls to zero in a less dramatic way, as one might expect in the presence of a boundary layer (see Appendix A, §A.1).

Some authors have posited the existence of an inner jet on the $r = 0$ axis (e.g., KLB), rather than set up an initial hydrostatic state. This is done to mimic the possible existence of a jet from a rotating central object in its own right. As already discussed, we have seen that numerically driven jet-like outflow can arise if care is not exercised in setting up an initial hydrostatic state. Given the sensitivity of all calculations to boundary conditions on the axis, we feel it is imperative to establish the existence of an inner jet by a calculation that specifically includes all the complexities of a central, magnetised, rotating body, rather than just assuming it, or possibly creating it with numerical truncation errors.

The external MHD torque on the disk, ultimately responsible for the disk wind, requires that a plausible threading magnetic field configuration be introduced. There are many possible choices, and we select among those that can be easily initialised within the ZEUS framework. In the previous 2-D work, current-free (and therefore force-free) configurations ($\mathbf{J} = 0$), were used, so as not to disturb the equilibrium of the hydrostatically stable corona.

The most obvious choice is a constant vertical magnetic field ($B_z = \text{constant}$), as used in OPII. OPI described the results of launching a jet into a non-uniform (but still force-free) magnetic field, consistent with what one would expect from a conducting plate in a vacuum in axisymmetry (Cao & Spruit 1994). Because the magnetic field lines in the configuration do not follow the grid axes, it is necessary first to evaluate the ϕ -component of the vector potential (A_ϕ), and then from this, determine the r - and z -components of the magnetic field (technical details for a similar problem are given in Appendix A, §A.3). Only in this way can the initial magnetic field be established with a zero divergence everywhere on the grid to within machine round-off errors.

Given that the 3-D simulations in the present paper are performed on a Cartesian, rather than a cylindrical co-ordinate system (see §3.2), we chose to simulate the behaviour of jets launched in an initially uniform magnetic field, parallel to the vertical z axis. This is far simpler than implementing the axisymmetric, potential configuration of Cao & Spruit (1994) in 3-D because of the difficulties in having to deal with three components of the vector potential⁵. Further, as seen in OPI and OPII, the vertical magnetic field model is, in many ways, more interesting.

2.1. Parameters of the Model

Our physical model treats the accretion disk as a set of fixed boundary conditions for the atmosphere. Thus, the values of five flow variables must be prescribed at every point of the accretion disk surface at all times (see also KLB). These five variables include the mass density, $\rho(r)$; two components of the magnetic field \mathbf{B} , namely $B_z(r)$ and $B_\phi(r)$ [$B_r(r)$ is fixed by the solenoidal condition]; and finally, two components of the velocity field, namely $v_z(r)$ and $v_\phi(r)$ [$v_r(r)$ in the disk is taken to be zero]. Note that the product ρv_z prescribes the mass loss rate per unit area from the disk, or, equivalently, the mass loading of field lines, and this quantity remains fixed throughout our simulations. We chose the value of the vertical speed, v_z , to be far less than the sound speed of the disk and the expected, slow magnetosonic velocity. Thus the resulting disk wind, if it achieves steady state, is accelerated through all three critical points (see OPIII for detailed discussion). We retain exactly this approach in establishing the disk conditions in our full 3-D problem.

Therefore, the length scale, r_i , density of the corona, ρ_i , and Keplerian velocity of the disc, $v_{K,i}$, are all taken to be unity at the inner edge of the disc. Thus, the time scale is in

⁵More elaborate magnetic field configurations can be implemented/initialised using the *JETSET* tool developed in Jørgensen et al. (2001).

units of $t_i = r_i/v_{K,i}$. The rest of the variables are set by using the functional forms given by equations (1), and by setting five basic parameters introduced in OPI. These are discussed below.

First, while we assume that the disc and corona are in pressure balance everywhere along their common boundary, there is a density jump (and thus a contact discontinuity) and this is given by the first parameter η_i , the ratio of the disc density to corona density at the inner radius ($r = 1$).

Second, while not critical to the ultimate launching of the jet, we do introduce a force-free toroidal magnetic field *in the disc only*. In part, this is done to reduce the gradient in B_ϕ across the disc-corona boundary, once the coronal toroidal field is established. To remain force-free, we choose the form:

$$B_\phi = -\frac{\mu_i}{r}, \quad (2)$$

where μ_i is the second parameter, and is equal to the desired ratio B_ϕ/B_z at $r = 1$.

Third, the vertical velocity v_z which provides the mass loading of the coronal magnetic field, is given by:

$$v_z = v_{\text{inj}}v_\phi, \quad (3)$$

where v_ϕ is the rotation velocity profile (mostly Keplerian) of the disc (Appendix A, §A.1) and v_{inj} is the third parameter.

Fourth, the ratio of Keplerian to thermal energy densities is given by:

$$\delta_i = \frac{v_{K,i}^2}{p_i/\rho_i} = \frac{1}{p_i}, \quad (4)$$

since $v_{K,i} = 1$ and $\rho_i = 1$. It is well known that for thermal atmospheres in hydrostatic balance, this ratio is given by $\delta_i = \gamma/(\gamma - 1) = 5/2$ for a $\gamma = 5/3$ gas. However, OPI argued from observational data that only a small fraction of the total pressure can be thermal in origin, and the rest must come from some other isotropic mechanism, such as Alfvénic turbulence. OPI considered the total pressure to originate from two terms, one thermal, the other turbulent, but since they modelled the Alfvénic turbulent pressure with the same $\gamma = 5/3$ polytrope used for the thermal component, the two components became physically indistinguishable. Thus, whether one thinks of the total pressure as being thermal plus Alfvénic, or all thermal, the numerical solutions are identical. Therefore, in the present work, we retain δ_i for consistency with OPI and OPII, but note that it simply refers to the inverse of the portion of the pressure designated as thermal. In any case, the total pressure at r_i is equal to $(\gamma - 1)/\gamma$.

Finally, the fifth parameter is the plasma beta, β_i , given as usual by:

$$\beta_i = \frac{2p_{t,i}}{B_{z,i}^2}, \quad (5)$$

where $p_{t,i}$ is the initial thermal pressure at r_i , and where the factor of μ_0 (or 4π , depending on one’s units of choice) has been absorbed into the scaling for the magnetic field. Since $p_{t,i} = 1/\delta_i$, we have:

$$B_{z,i} = \sqrt{2/\delta_i\beta_i}. \quad (6)$$

In the five 3-D simulations presented herein (see §3.3), the values for these five parameters are the same as in OPII, namely:

$$(\eta_i, \mu_i, v_{\text{inj}}, \delta_i, \beta_i) = (100.0, 1.0, 0.001, 100.0, 1.0). \quad (7)$$

3. 3-D SIMULATIONS

3.1. Computational Details

The 3-D simulations were computed with ZEUS-3D, a multi-dimensional, finite-difference, Eulerian MHD code developed by D.A.C. While sharing a common lineage with the NCSA’s public-domain code of the same name, our code uses different algorithms for solving the induction and momentum equations, namely, the *Consistent Method of Characteristics* (CMoC, see Clarke 1996 for details).

Like all codes in the ZEUS family, our version of ZEUS-3D uses a staggered mesh to reduce the number of interpolations required at the zone faces. Interpolations are performed with the second-order accurate scheme first proposed by van Leer (1974). It uses an operator-split, time-centred algorithm for transporting the variables and applying the source terms.

The CMoC algorithm sets our code apart from its predecessors. It uses a planar-split strategy, rather than the traditional directional splitting employed by earlier versions of the code (e.g., Stone & Norman 1992a; Hawley & Stone 1995). In addition, the magnetic induction, momentum transport, and transverse Lorentz acceleration are all tightly coupled by using the same interpolated values of \vec{B} and \vec{v} . It is a robust algorithm, and possesses no known numerical instabilities or problems in 3-D.

Three relatively minor modifications were made to the code in order to perform the simulations discussed in the next sections. First, in order to “turn off” the internal energy equation and implement the polytropic equation of state, we simply replaced the pressure gradient terms in the momentum equation with gradients of the function $\rho^{\gamma-1} + \Phi$, where ρ

is the updated density distribution, and Φ is given by equation (1) at all time steps. Since the internal energy equation contributes to the dynamics only via the pressure gradient in the momentum equation, this is all that has to be done to affect this change. For example, other than for computational efficiency, there is no need to prevent the code from updating the internal energy (e); it is simply never used.

Second, since the internal energy variable is ignored, it is necessary to modify the dependence of the CFL time step on the sound speed. Thus, instead of computing c_s from e and ρ [i.e., $c_s^2 = \gamma(\gamma - 1)e/\rho$], we use $c_s^2 = \gamma\rho^{\gamma-1}$, thereby introducing the polytrope explicitly.

Third, a subroutine is required to initialise the corona (all flow variables, including the gravitational potential) and the disc boundary according to the discussion in the previous section.

Other changes of a more technical nature were required to address boundary condition problems, special graphics, and other such things. As mentioned in §2.1, the hydrostatic atmosphere is very prone to numerical instabilities, particularly at the boundary, and we found these problems to be even more significant in 3-D. These details are relegated to Appendix A.

3.2. Initialising the Simulations

Contrary to what may be intuitive, it is inadvisable to perform a 3-D simulation such as this in cylindrical coordinates. For one thing, special treatment must be introduced for the “wedge zones” that abut the z -axis (no longer a symmetry axis in 3-D), and velocities that pass through the z -axis pose a very difficult numerical problem. Second, even with such technical details solved, plane waves are badly disrupted upon passing through the z -axis (John Hawley, private communication), and this provides an undesirable bias to what should be an unbiased three dimensional calculation⁶.

Thus, we use Cartesian coordinates, (x, y, z) , for these simulations. The disc is taken to lie along the x - y plane, and the disc axis corresponds to the z -axis (see Fig. 1). While Cartesian coordinates are the natural system to use to avoid any directional biases, it does introduce some of its own problems not encountered in the 2-D cylindrically symmetric simulations, and we discuss these further in Appendix A.

Five separate 3-D simulations were performed for this work, and their details are sum-

⁶By unbiased, we mean that no axis should be preferred numerically in any way over another.

marised in Table 1. Simulations A, B, C, and E were all performed at the same resolution and same spatial extent, while simulation D was performed with a slightly larger spatial extent and with twice the radial resolution as the other four runs. In this paper, we concentrate primarily on simulations D and E.

In units of the inside radius of the disc, r_i , the *primary* computational domain of runs A, B, C, and E have dimensions $(-15 : 15, -15 : 15, 0 : 60)$, and is divided into $(60, 60, 120)$ uniform cubical zones. Thus, there are only two zones between the disc axis and the inner radius of the disc. This should be compared with the 2-D runs of OPI and OPII which, using cylindrical coordinates (z, r) , was computed over a domain $(0 : 80, 0 : 20)$ and resolved with $(500, 200)$ zones (and thus ten zones per r_i). By comparison, therefore, these 3-D simulations have one fifth the resolution of the 2-D runs.

The primary computational domain of run D has the same physical extend as the 2-D runs in OPI, namely $(-20 : 20, -20 : 20, 0 : 80)$, and is divided into $(100, 100, 160)$ zones. Along the z-axis, the zoning is uniform, and thus has the same axial resolution (two zones per r_i) as the lower resolution runs. However, along the x - and y -directions, 40 uniform zones resolve the range $\pm 5r_i$ (giving a radial resolution in the vicinity of the disc axis of 4 zones per r_i), while 60 “ratioed” zones are used to resolve the remainder of the range $(-20 : -5$ and $5 : 20)$. At $r = 15$, the radial extent of the zones has grown to about $0.6r_i$ (comparable to the lower resolution runs), and at $r = 20$, to about $0.9r_i$. Thus, resolution far away from the disc axis has been sacrificed to some extent in favour of higher resolution in the more important regions nearer the disc axis.

Figure 1 shows a schematic of the setup of our grid for runs A, B, C, and E. The *primary* computational domains of all simulations are embedded in a *greater* computational domain which, for runs A, B, C, and E, is $(-30 : 30, -30 : 30, 0 : 120)$, while for run D, is $(-40 : 40, -40 : 40, 0 : 160)$. The portions of the greater domains that lie outside the primary domains are resolved with 10 to 20 severely ratioed zones, and are never used for analysis. They are merely there to act as a “buffer” between the primary computational domain and the imperfect outflow boundary conditions (see Appendix A, §A.4 for further discussion).

We use inflow boundary conditions at the $z = 0$ boundary (disc), even inside the inner disc edge. However, because the azimuthal velocity profile, v_ϕ [equation (A.2)], goes to zero inside $r = r_i$ and because the inflow velocity, v_z , is set to a fraction of v_ϕ , actual inflow is restricted to the portion of the boundary where $v_\phi \neq 0$, namely the putative disc. In addition, because the Cartesian grid is rectangular, numerical problems arise near the corners of the grid if rotation of the fluid is permitted to persist there (Appendix A, §A.1). Thus, the Keplerian profile of the disc is reduced smoothly to zero between an “outer radius” (r_o),

which roughly corresponds to the radius of the smallest cylinder that can fully contain the primary computational domain, and r_{\max} , chosen to be greater than r_o but still less than the maximum extent of either the x - or y -axes (see equation A.2 in Appendix A). Note that because r_o lies outside the primary computational domain, the truncation of the Keplerian profile at r_o has no visible effect within the region of analysis (namely the primary domain).

As described, the corona and disc possess quadrantal symmetry, and runs A, B, and C were designed to determine the best way of breaking this. Run A was set up with the identical parameters and boundary conditions as the 2-D run in OPII, without any deliberate attempt to break the quadrantal symmetry. In principle, 2-D slices through this run should be very similar to lower resolution 2-D runs from OPII, and until $t = 150$, this was indeed the case. However, quadrantal symmetry is not the same as cylindrical symmetry, and their differences show up in the latter half of the simulation. Still, the jet remained centred about the disc axis and propagated at roughly the same velocity as observed in 2-D.

In run B, the quadrantal symmetry was broken by offsetting the centre about which the velocity profile of the disc is computed relative to the centre of the gravitational potential (located at the grid origin). Initially, the offset (one to tens of percent of r_i , it does not seem to matter) is along the x -axis and at $t=10$, is “jerked” to the same position along the y -axis. Meanwhile, in run C, the disc is effectively wobbled, rather than being jerked. Details of how the jerk and wobble are implemented are found in Appendix A (§A.2).

Qualitatively, runs B and C are identical, and the quantitative differences are slight. However, both simulations are completely different from run A, in which nothing deliberate was done to break the symmetry. Thus, we conclude that it does not really matter how the quadrantal symmetry is broken, so long as it is broken. Run D is the same as run C but at a higher resolution and is discussed further in §4. No further discussion will be given for runs A, B, and C.

Run D uses the same radial profiles for the velocity, magnetic field, and density in the disc as OPII. In particular, at the inner radius of the disc, the Keplerian velocity profile is suddenly truncated, leaving a cusp in v_ϕ at $r = r_i$ (Fig. 2, see also Appendix A, §A.1). Run E, therefore, was designed to test the dependence of the numerical results on how the Keplerian velocity profile is truncated at $r = r_i$. In particular, in run E, we use the region between $r = \frac{1}{2}r_i$ and $r = 2r_i$ to round off the Keplerian velocity profile smoothly to zero (Fig. 2). Thus, in run E, there is no cusp in the profile for v_ϕ and the amount of angular momentum transferred from the disc to the corona is significantly less than that of run D. We find that this gives qualitative differences in the relative importance of the various modes of the K-H instabilities that are excited (see §5).

The greater computational domains of runs A, B, C, and E include about 900,000 zones and required about 9,000 MHD cycles and 50 hours of CPU time on an IBM Power 3+ processor to run to $t = 300$ (in units of $r_i/v_{K,i}$). For contrast, the greater computational domain of run D included nearly 2.9 million zones and required about 22,000 MHD cycles and 18 *days* on the same machine to run to $t = 400$. In all cases, the simulation was terminated once the working surface of the jet left the greater computational domain, and/or when the effects of the imperfect outflow boundary conditions made themselves felt on the primary computational domain.

Finally, the differences between runs C and D were surprisingly slight, affecting primarily the details of the profile of the jet. Thus, we justify using the lower resolution setup for run E, and performing a simulation that took two days rather than eighteen.

Simulation	primary domain (r_i)	greater domain (r_i)	r_o/r_i	r_{\max}/r_i	symmetry breaking	inner v_ϕ profile
A	$30 \times 30 \times 60$	$60 \times 60 \times 120$	22	28	none	truncated
B	$30 \times 30 \times 60$	$60 \times 60 \times 120$	22	28	jerked	truncated
C	$30 \times 30 \times 60$	$60 \times 60 \times 120$	22	28	wobbled	truncated
D	$40 \times 40 \times 80$	$80 \times 80 \times 160$	30	38	wobbled	truncated
E	$30 \times 30 \times 60$	$60 \times 60 \times 120$	22	28	jerked	smooth

Table 1. Specifics of the five simulations performed in this work. The numerical resolution of the primary domains for simulations A, B, C, and E was $60 \times 60 \times 120$ zones, while for simulation D, $100 \times 100 \times 160$ zones. The “truncated” and “smooth” profiles for v_ϕ are shown in Fig. 2.

4. A “CORKSCREW” JET

We first focus on simulation D, which other than dimensionality and resolution, was initialised in the same way as the simulation discussed in OPII.

The quantities illustrated in false colour in Figs. 3a and 3b are respectively:

$$\int \rho(l) dl, \quad \int \nabla \cdot \vec{v}(l) dl,$$

where $\rho(l)$ and $\nabla \cdot \vec{v}(l)$ are the density and velocity divergence at coordinate l integrated along the line of sight. Thus, Fig. 3a is a 2-D map of the column density in the primary

computational domain, while Fig. 3b indicates regions of compression (blue) and expansion (red) along the line of sight. In both cases, the z -axis of the data cube has been rotated by 20° out of the visual plane. The image is taken at $t = 320$, and is representative of the appearance of the jet from $t = 210$ through $t = 400$. The disc (not visible in this rendering because boundary values are not included in the line-of-sight integrations) is at the left hand side of the image, and outflow is from left to right.

Figure 3a shows that the jet has settled into a quasi-steady state structure in the shape of a single helix, or a “corkscrew”, and the bulk of this section is devoted to explaining how the jet reaches this configuration. On the primary computational domain, there are roughly 1.2 wavelengths of the helix, the wavelength itself depending on the complexities of the K-H instabilities ultimately responsible for the structure. The line-of-sight integration of the velocity divergence (Fig. 3b) is included because it nicely illustrates the most dynamic portions of the helical jet (two narrow blue ribbons on either side of the material jet visible in Fig. 3a indicating regions of greatest compression) twisting around a relatively stable, slightly expanding core (red). One must be careful in interpreting the velocity divergence as shocked regions, since the polytropic equation of state precludes the Rankin-Hugoniot jump-conditions. Thus, Fig. 3b is included for illustrative purposes only.

4.1. The Nature of the Outflow

Figure 4 shows a time-series of eight contour plots of density taken along the y - z plane, where the z -axis (horizontal) corresponds to the axis of the disc. In these slices, the $+x$ -axis, located at $y = z = 0$, points into the page. The eight epochs chosen are $t = 20, 60, 100, 160, 200, 240, 320$, and 400 . In Fig. 4a, the vertical lines mark the location of the cross-sectional cuts shown in Figs. 7–10. Figures 5 and 6 are similar montages for the normal magnetic field (B_ϕ) and poloidal velocity vectors respectively.

As in 2-D, a global Alfvén wave is launched from the disc as the rotation twists the initially uniform and vertical magnetic field in the corona. By $t = 20$, this wave has propagated a third of the way across the grid (Fig. 5a) and the collimated outflow has reached about $z = 10$ (Fig. 4a). Until $t = 100$, the jet behaves much like the 2-D jet reported in OPII as the non-axisymmetric modes have not grown enough to break the initial cylindrical symmetry. Thus, knots are generated in the same way they were in 2-D in response to the early appearance of the $m = 0$ pinching mode of the K-H instability⁷ (e.g., the four symmetrically

⁷We remind the reader that $m = 0$ K-H mode pinches jets (“sausage” instability), but does not disrupt them. This is the only mode that can be excited in 2-D axisymmetry. In 3-D however, helical modes ($m = 1$)

positioned knots near the head of the advancing jet, each labelled with an ‘H’ in Fig. 4c).

By $t = 120$ (not shown), the weak $m = 0$ knots forming along the jet axis have all but merged back together, as the differences between the cylindrical and near-quadrantal symmetries start to appear. In particular, while *only* the $m = 0$ mode can appear in a cylindrically symmetry system, all modes that are multiples of four will appear in a quadrantly symmetric system, and the $m = 4$ mode begins to dominate the $m = 0$ mode after $t = 100$. Figures 7 through 10 show x - y profiles at $z = 30$ (indicated by the vertical line in Fig. 4a) for the density, Alfvénic Mach number, velocity, and magnetic field (in the latter two, contours indicate the normal component, vectors indicate the poloidal component). The quadrantal distortion ($m = 4$ mode) is clearly evident in panels d, e, and f of Figs. 8 and 9.

By $t = 160$, the effects of breaking the quadrantal symmetry are evident, as a clear sinusoidal distortion finally appears along the jet axis (Figs. 4d, 5d, and 6d). This is the beginning of the $m = 1$ mode of the K-H instability, and represents the greatest threat to the ultimate stability of the outflow.

A brief recap of the various modes of the Kelvin-Helmholtz instability encountered so far is in order. First, Hardee, Clarke & Rosen (1997) show that while the $m = 0$ mode is the fastest growing mode, its amplitude is always less than that of the $m = 1$ mode, whose amplitude is greater and whose growth rate is faster than all the other modes ($m \geq 2$). Thus, it is not surprising that we should first see hints of the $m = 0$ mode discussed in OPII before the onset of the $m = 1$ mode. What may be surprising, however, is the appearance of the $m = 4$ mode before the $m = 1$ mode.

In fact, the development of the two modes arises from very different processes. The $m = 1$ mode arises entirely from the growth of signals propagating from the left-hand boundary (e.g., the disc wobble). On the other hand, the $m = 4$ mode arises from *in situ* perturbations associated with the fact we are resolving a rotating, initially cylindrically symmetric object on a Cartesian grid. Thus, the $m = 4$ mode appears well before the $m = 1$ mode because the driver of the $m = 4$ mode are grid truncation errors which exist over the entire domain.

are dominant and can threaten the integrity of a jet. The higher order “flute” modes ($m \geq 2$) corresponding to elliptical ($m = 2$), triangular ($m = 3$), rectangular ($m = 4$), etc. modes, do not end up destroying a jet, although they can strongly affect the cross-section of the jet and split it into m separate beams [see e.g., (Ray 1981)]. Recall as well that the radial structure of modes in jets are of two general types, namely surface modes (which are localised towards the surface of the jets) as well as body modes (involving the whole body of the jet). Analytical calculations of simple jet models predict that the growth rates of surface modes exceeds that of the body modes (see Gill 1965, for discussion).

Regardless of what drives the modes, however, once initiated, they will be tracked in a physical manner by the numerics, and eventually, the faster-growing $m = 1$ mode comes to dominate the structure. Thus, by $t = 200$, the jet has responded to the $m = 1$ mode by adopting a helical, or “corkscrew” morphology from $z = 30$ and beyond. In Fig. 4e, the impression is that the collimated jet ends at $z = 30$, after which the jet has broken up into two distinct clumps, one at $(y, z) \sim (-7, 38)$, and the other at $(y, z) \sim (13, 66)$. In reality, the jet remains contiguous throughout the simulation, and the “clumps” are simply the intersection of the helical jet with the viewing plane.

The corkscrew advances in time (i.e., rotates in the same direction as its twist) and by $t = 240$ (Figs. 4f and 5f), the base of the corkscrew has shrunk to $z = 15$. Three cross sections of the corkscrew (and thus more than an entire wavelength) are now contained within the primary computational domain [the third “clump” just entering the right-hand boundary⁸ at $(y, z) = (-4, 80)$], and the centre of the jet has now moved nearly a full jet diameter from the disc axis (Fig. 7f). Thus, no part of the jet contains any of the original symmetry axis, whence our designation “corkscrew”.

In the cross-sections at $z = 30$, (Figs. 7–10), one can see the progression from the dominance of the quadrantal $m = 4$ mode (e.g., Figs. 8d, 8e, and 8f) to the helical ($m = 1$) mode (e.g., Figs. 8g and 8h). At this location, much of the effects of the early $m = 4$ mode have disappeared by $t = 320$, while at higher values of z (not shown), the effects of the $m = 4$ mode dissipate significantly earlier (e.g., at $z = 50$, there is little sign of the $m = 4$ mode by $t = 200$). In panels f, g, and h of Figs. 7 and 8, steep gradients (indicated by “contour bunching”) effectively demarcate the cross section of the jet which is predominantly elliptical, although evidence of higher order ($m > 2$) fluting instabilities are apparent in the jet profile. Meanwhile, and most significantly, the cross section of the magnetic field (Figs. 10g and 10h) shows that a strong axial magnetic field has developed inside the centre (i.e., nearer the z -axis) of the displaced jet (c.f., Fig. 7g and 7h), and this acts as a backbone providing stability to the jet.

By $t = 320$ (Figs. 4g, 5g, and 6g), the corkscrew continues to advance, and has now consumed all but the inner several r_i of the jet. The wavelength of the corkscrew gradually lengthens, but the overall displacement of the jet from the disc axis remains at about one jet diameter (e.g., Fig. 7g), with the displacement increasing toward the disc. Between $t = 240$ and $t = 320$ (e.g., Figs. 7f and 7g), the corkscrew has rotated about 180° in the

⁸Recall that the right-hand boundary is not really a boundary at all, since the “greater computational domain” extends to $z = 160$. Thus, having features and/or material enter from what is ostensibly an outflow boundary is quite acceptable, so long as that feature did not originate from the true outflow boundary at $z = 160$.

counterclockwise direction.

By $t = 400$ (Fig. 7h), the corkscrew has rotated by another 150° , and thus the rotation rate is not uniform in time. Further, the rotation rate is more rapid near the base of the corkscrew than it is further out. For comparison, at $z = 50$ (not shown) between $t = 240$ and $t = 400$, the helix advances by only 270° , compared to 330° at $z = 30$. As a result, the pitch of the helix is neither uniform nor constant. Further, severe $m \geq 2$ (elliptical and higher order) distortions can be seen in the jet profile in panel h of Figs. 7–9, and thus the shape of the jet profile is also highly dynamic. Nevertheless, the jet manages to maintain collimation throughout the simulation; outflow is never interrupted, nor significantly slowed.

4.2. How Do Corkscrew Jets Maintain Stability?

Typical outflow speeds along the jet range from 0.7 to 0.9 in units of the Keplerian velocity at $r = r_i$. We argue that if the jet can manage to configure itself in such a way that the Alfvén speeds are comparable to or higher than unity, then the jet will be sub-Alfvénic, and the K-H instabilities will be saturated (thereby satisfying linear stability conditions, e.g., Ray 1981). We now show that this Ansatz is precisely satisfied by the behaviour of the jet in simulation D.

Figures 7 and 10 show cross cuts of the density and magnetic field respectively. At all later times, $t \geq 240$, we see the body of the jet displaced by a jet diameter or so from the disc axis. While both the density and normal magnetic field cross sections show well-defined peaks, upon careful examination one finds that the peaks are not cospatial (e.g., compare Figs. 7g and 10g). This anti-correlation of density and magnetic peaks is found frequently in MHD applications, and the present authors have discussed this effect previously (Clarke, Norman & Burns 1986; OPII).

Corresponding to the peak in normal magnetic field are flux loops (shown as vectors in Fig. 10), and combined with the normal field, provide the jet with a “backbone” of relatively strong helical magnetic field. The density peak is then centrifugally driven toward the outside (away from the disc axis) of the backbone as the corkscrew advances in time.

At every slice along the jet at every epoch after $t = 220$, the density peaks always corresponds to the location of the highest Alfvén Mach number (high density and low magnetic field yields a low Alfvén speed), and these are typically of order 2 to 2.5. In contrast, the centre of the magnetic backbone corresponds to the lowest Alfvén Mach number (low density and high magnetic field yields a high Alfvén speed), and these are typically of order 0.1, or less. Averaged over the entire cross section of the jet, the Alfvén Mach number is of order,

or less than unity, and this is ultimately how the stability of the jet is maintained.

Thus, our explanation for the maintenance of jet stability goes as follows. At first, when the jet is launched, its internal dynamics are dominated by the 2-D symmetry described in OPII. The jet has no reason at the very early stages to respond to the $m = 1$ mode, as it is not present until $t = 160$. Thus, the initial distributions of density, magnetic field strength, and Alfvén Mach numbers are entirely determined by the nature of the disc and the corona.

However, the $m = 1$ mode does grow in time, and the jet must respond. It is not free to reduce its velocity, since this is determined by the forces at the base of the jet, and the jet begins to buckle under the stresses of the $m = 1$ mode. But by buckling, the magnetic field lines inside the jet are stretched, twisted, and thus strengthened. As this happens, portions of the jet become overpressured with magnetic pressure, squeezing out thermal material to restore total pressure balance inside the jet. This is ultimately responsible for the separation of the density and magnetic peaks, and as a result, portions of the jet attain very low Alfvén Mach numbers.

The jet continues to respond to the $m = 1$ mode by forming a helical structure, and as the amplitude of this structure increases, so does the strength of the magnetic backbone forming inside the jet, along with the average Alfvén speed. At some point, the mean Alfvén Mach number inside the jet is reduced to or below unity, not because of a reduction in flow speed, but because of the increase in Alfvén speed. Thus, the jet becomes sub-Alfvénic, and the K-H instability is saturated.

As seen in the simulation, this balance manages to maintain itself with slight variations and oscillations for nearly half of the computational time. While we cannot continue the present simulation any further than we have because of boundary effects creeping into the solution, it seems plausible that this balance should persist indefinitely, giving jets which are initially K-H unstable a characteristic helical, or corkscrew morphology.

Of course, not all jets are observed to be corkscrews, and one immediately asks whether there is any way to avoid such a morphology, given the evidence presented in this section that corkscrews are a natural configuration for a jet to assume in order to preserve stability. Simulation E discussed in §5 offers at least one scenario in which a jet manages to retain stability without attaining a large amplitude corkscrew morphology.

5. A “WOBBLING” JET

In this section, we focus on simulation E which we characterise as a “wobbling” jet because the centre of the jet never strays more than a jet radius away from the original symmetry axis. This simulation uses a smoothed Kepler velocity profile at the inner edge of the disk (Fig. 2), in contrast with simulation D which used the cusped profile. Simulation E produces a much richer structure in the jet, which prompted us to develop a Fourier transform analysis package (see <http://www.nordita.dk/~ouyed/JETTOOLS>) that could reveal the quantitative details of the modes that are excited within the jet.

5.1. Nature of the Outflow

Figure 11 (and 12) shows isodensity contours of simulation E in the y - z (and x - z) plane containing the disc rotation axis at $t = 50, 80, 120, 130, 150, 180, 210$ and 240 . By $t = 50$ (Fig. 11a and Fig. 12a), the Alfvén wave has moved off the right boundary and the jet has propagated nearly half way across the grid. The jet is driven by the field lines that are sufficiently displaced radially outwards (i.e., between $1 \leq r \leq 5$; the jet is hollow), which allows the centrifugal acceleration to occur, similar to what was observed in the 2-D simulations of OPII.

The jet at these early times is very stable, and accelerates to maximum velocities of the order of $0.7v_{K,i}$. This is somewhat slower than the 2-D counterpart (OPII) where velocities of the order of $1.2v_{K,i}$ were reached where mass entrainment is not as effective in slowing down the jet as it is in 3-D. The flattening (Figs. 11c, 11d and 11e) and stretching (Figs. 12c, 12d and 12e) of the jet is evident as well as its response to the kink mode (Figs. 11f, 11g, 12f and 12g; see also §5.2.1) before it eventually regains a nearly cylindrical morphology centered on the disc axis (Figs. 11h and 12h).

The distortion of the cross-sectional shape of the jet is shown in Fig. 13, which displays isodensity contours in the x - y plane located at the vertical line in Fig. 11a. The jet’s cross-section becomes increasingly elliptical from $t = 80$ onward, and evidence of higher-order fluting modes becomes apparent by $t = 120$. The highly elliptical cross-section appears to break apart into separate streams at $t \sim 150$. This behaviour is strongly suggestive of the non-linear evolution of an $m = 2$ elliptical mode (see below). We see that this highly elliptical, and even bar-like distortion, gradually fades away, so that at $t \geq 200$, the jet profile appears to be more cylindrically symmetric in the main, with the exception of an obvious, one-sided bar-like protrusion that is suggestive of a residual $m = 1$ helical mode.

The elliptical cross-section of the jet in Fig. 13 precesses until $t = 130$, and then appears

to remain fixed in position angle until $t = 200$. This is indicative of equal amplitudes in the $m = \pm 2$ elliptical modes, discussed further in the next subsection. The precession of the jet cross-section resumes after $t = 210$.

Figure 14 shows the evolution of 20 magnetic field lines at $t = 50, 80, 120, 130, 150, 180, 210$ and 240 . The lines were chosen to visualise best the complex dynamics in the jet. The two central magnetic field lines (dotted lines) originate from the central compact object inside $r = r_i$ and trace the poloidal field lines that ultimately serve as a “backbone” for the jet.

The structure of the jet magnetic field remains well-ordered until $t \simeq 80$. Before this time, the inner two field lines remain rather straight, indicating that the axis of the jet is quiescent. The inner-most field lines attached to the disk have a clearly helical structure as these are associated with the jet itself. The outer-most field lines are beyond the collimated outflow and are affected only by the slow rotation of the corona. As such, they are strongly poloidal in character.

The jet’s axis, as well as its helical structure, become more disorganised at $80 < t < 210$ and execute both a long-wavelength, transverse wandering, as well as shorter-scale, disorganised motions. It is clear however, that the jet survives this unstable behaviour and appears to resume its initial ordered, regular character at $t > 210$. Throughout it all, the acceleration region of the outflow close to the disk remains largely unaffected.

Figure 15 shows 20 individual streamlines in the jet at the same epochs as in Fig. 14. We note that in general, time-dependent flow, streamlines are not restricted to flow along surfaces of constant magnetic flux, and hence do not follow field lines, as is apparent when comparing Figs. 14 and 15. Streamlines at $t \simeq 50$, and later at $t \geq 210$, show an ordered, helical outflow. Between these times however, note the disorder of the flow as various modes of instability play themselves out in the evolution of the jet.

Figure 16 shows the velocity vectors in the same $y-z$ plane as Fig. 11. and further illustrates the effect of the kink mode on the body of the jet (Fig. 16e and Fig. 16f) before it regains its coherence and cylindrical (one stream) shape in Figs. 16g and 16h. Figure 17 shows the velocity vectors in the same $x-y$ plane as Fig. 13. One sees that the ordered rotation of the jet (a consequence of the fact that it is carrying off the angular momentum of the driving disk) is present up to $t = 80$. This gives way to far more disorganised motion between $80 < t < 210$. In Figs. 17g and 17h, we see that an ordered, nearly circular rotational motion is re-established in this plane. This reflects the behaviour of the streamlines in Fig. 15. Finally, this evolution of jet rotation is qualitatively similar to what was seen in Fig. 9 for the corkscrew jet (simulation D, §4).

Thus, the jet begins as a stable outflow, destabilises between $80 < t < 210$, and then resumes some decorum of stability after $t = 210$. The instability at intermediate times appears to be driven by the excitation of a number of discrete K-H modes $m > 0$. The region close to the disk, being characterised by sub-Alfvénic flow, remains reasonably quiet throughout the simulation. Thus, as with the corkscrew jet, the wobbling jet manages to survive the onset of potentially destructive non-axisymmetric modes, and this is investigated in the next sub-section.

5.2. How do Wobbling Jets Maintain Stability?

We decompose the radial structure of the jet by performing a Fourier transform (see <http://www.nordita.dk/~ouyed/JETTOOLS>) of the 2-D pressure distributions (not shown, but qualitatively similar in appearance to the density distribution shown in Fig. 13). Our results are shown in Fig. 18 where we plot the amplitude of a mode with radial wave number k_r and azimuthal wave mode number, m . (k_r is measured in units of $(10r_i)^{-1}$). The grey scale ranges from high amplitude (white), to moderate amplitude (grey), and down to low amplitude (black).

5.2.1. Onset of Kelvin-Helmholtz Modes

As observed for the corkscrew jet, we find that the $m = 0$ mode is the predominant mode at early times, $0 \leq t \leq 80$, corresponding to when the initial cylindrical symmetry of the initial setup survives. Indeed, the high density (and pressure) region of the jet (Fig. 13) is nearly circular at these times. The $m = 0$ mode reappears at later times ($t \geq 210$) when the jet cross-section is again nearly circular.

The elliptical, $|m| = 2$, modes⁹ responsible for the elliptical cross-section of the jet (Fig. 13), first appear at $t = 80$, and persist until $t \sim 210$. We note that the amplitude of both the $m = -2$ and the $m = 2$ elliptical modes in Fig. 18, are nearly the same for most times, and this freezes the position-angle of the elliptical cross-section in space, as noted in §5.1. The $|m| = 2$ modes ultimately grow enough to cause the jet to bifurcate between $120 < t < 180$.

⁹There are two senses of rotation for each m -mode of a cylindrical jet. Thus, $m > 0$ and $m < 0$ correspond to waves that wind around the jet axis in either the same or the opposite sense as the toroidal magnetic field respectively.

The higher order, $|m| = 4$, modes appear slightly after the $|m| = 2$ modes starting at $t = 120$, and disappear again at $t \simeq 180$. They manifest themselves by giving the cross-section a marked rectangular appearance, such as in Figs. 13c and 13d. As before, these are excited, in part, by the initially cylindrical symmetric atmosphere rotating within a quadrantally symmetric grid.

The $|m| = 1$ modes makes their first strong debut (relative to the amplitude of the flute and pinch modes) rather late in the evolution of the jet, at $t \simeq 150$. The helical mode is of comparable amplitude to the elliptical modes, so the jet’s cross-section still remains rather elliptical in shape.

It is clear from Fig. 18 that for $150 < t < 210$ the jet’s evolution is dominated by the $m = 1$ and $m = -1$ modes, with the higher order flute modes diminishing in importance. We also note that the amplitude of the $m = 1$ mode is always greater than that of its $m = -1$ counterpart. This is why the late-appearing, bar-like protrusion noted earlier undergoes its slow rotation.

A global view of Fig. 18 shows that the various modes that are strongly in play at $t = 120$, gradually damp out in their amplitude. By the end of our simulation, at $t = 240$, there is a bit of activity in the $m = 1$ mode. This “spectrographic” image of the jet’s evolution shows that the jet has survived the instability, and that the potentially unstable modes all damp down with time. The jet has all but evaded the most threatening instability. A second general trend apparent in Fig. 18 is that the radial wavenumber of the unstable modes becomes smaller, that is $k_r \rightarrow 0$ (e.g., compare Fig. 18b with 18h). The increasing radial wavelength of the modes with time shows that the jet is regaining its coherence from a beam that was broken into two separate streams to a single coherent stream again at the end of the simulation.

5.2.2. *Stabilising the Wobbling Jet: Transition to Sub-Alfvénic Flow*

Figure 19 shows the time evolution of the Alfvén Mach number (M_A) along the innermost magnetic field line ($r = r_i$) at $50 \leq t \leq 240$. In these panels, the value of M_A is plotted as a function of the position s along the field line. The vertical dashed line in any frame indicates the point s_A along the field line at which the flow reaches the Alfvén point (where $M_A = 1$).

Up to $t = 80$, the maximum value of M_A continues to increase beyond the Alfvén point, to a maximum of $M_A = 4$. The position of the Alfvén point is at $s_a \simeq 12$ – 15 at these earlier times. At $t > 80$, we see that the maximum value of M_A decreases systematically with time. At $150 \leq t \leq 210$, the velocity of the flow on this entire field line is sub-Alfvénic. We note

that $t = 150$ in Fig. 19 is approximately the time where the $|m| = 2$ modes begin to fade out.

This decrease in M_A along the field line begins at almost the same time as the appearance of the non-axisymmetric modes in the jet. We note that the reappearance of super-Alfvénic flow at $t \geq 210$ is the time in which only low level $|m| = 1$ modes are left, as discussed above. Our results show therefore that the appearance of unstable modes in the jet is directly correlated with the Alfvénic Mach number of the jet.

The instability breaks out when the jet becomes super-Alfvénic. However, the jet Alfvén Mach number is systematically reduced as a consequence of the unstable modes. The modes begin to lessen in strength as soon as the Mach number decreases below unity. This is excellent evidence that flow stabilisation occurs as a consequence of the mechanism that de-stabilises the jet in the first place. Once again, we see that the jet is self-regulating in the sense of being able to adjust its structure to preserve conditions of stability.

Figure 20a shows the time evolution of the mean average toroidal magnetic field in the jet. The toroidal field builds in amplitude while the jet is stable, reaching a peak at $t = 50$. It decreases with time beyond this until $t \simeq 130$ and remains at this lowest value until $t \simeq 180$ whereupon it starts a steady and monotonic rise to a maximum value achieved at the end of the simulation.

The overall energetics of the jet are shown in Fig. 20b. Despite the fact that B_ϕ decreases between $50 \leq t \leq 130$, the total magnetic energy systematically increases because of an increase of the strength of the poloidal field component caused by the stretching of field lines by the unstable $|m| = 1$ and higher order fluting modes.

The fact that the magnetic energy taps into the bulk kinetic energy of the flow (which includes energy stored in the K-H modes) is apparent in Fig. 20b, where between $t = 130$ and $t = 170$, E_m rises as E_k falls. Just as in the case of the corkscrew jet, the sheared velocity field in the jet is the ultimate source of the energy tapped by the unstable modes and transferred into poloidal field, stabilising the jet against the $|m| = 1$ modes.

After $t = 180$, the kinetic energy grows at the expense of the magnetic tension in the poloidal field, and the jet is efficiently accelerated to super-Alfvénic flow once again. This quasi-periodic transfer of energy between kinetic and magnetic fields suggests that the jet may oscillate between quasi-stable and quasi-unstable epochs as it propagates into its surrounding environment. Unfortunately, our simulation could not be carried out long enough to confirm this hypothesis, because effects of the outflow boundary conditions were beginning to creep into the primary computational domain.

6. DISCUSSION AND CONCLUSIONS

We have presented results from a numerical study of a variety of different simulations of 3-D winds from accretion disks threaded by vertical field lines. Although, our present simulation is far from the high resolution used in previous 2-D simulations (OPI and OPII), we find that the acceleration phase of the jet is very similar.

Our set of simulations suggests a general stabilisation mechanism independent of how the jet is perturbed, and on the nature of the boundary conditions employed. The most fascinating result of our simulations is that jets in 3-D, while manifesting the expected unstable modes long discussed in the literature, remain stable. This remarkable behaviour can be traced to the self-limiting action of the instability itself. The jet becomes unstable in regions of high Alfvén Mach number, as both analytical and numerical studies of much simpler jet systems have suggested (e.g., Ray 1981; Hardee & Rosen 1999). The appearance of the $|m| = 1$ modes pump energy into the poloidal magnetic field, causing the jet Alfvén Mach number to fall below unity and stabilise the jet. The unstable modes die away, and the flow can once again start to accelerate to Alfvén Mach numbers greater than unity.

The differences between simulations D and E can be traced to the different v_ϕ profiles imposed at the accretion disc (Fig. 2). In short, the cusped profile used in simulation D moves more specific angular momentum per unit time onto the grid than the smoothed profile of simulation E. Thus, the $m = 1$ mode is highly dominant in simulation D, driven by the high angular momentum of the inner parts of the corona. In contrast, this driver is subdued in simulation E, and other modes of the K-H instability are manifest. The simple $m = 1$ dominance in simulation D leads to the corkscrew morphology in which the jet achieves a balance between the centrifugal and magnetic stresses (very similar to OPII explanation for the $m=0$ mode in the 2-D jet, and the knot generator). With lots of modes playing a role, the dynamics are much more complex in simulation E.

Above all, the critical point is that despite the differences in boundary conditions, both jets manage to strike a balance and avoid disruption by the many modes dumping energy into the magnetic field.

The development of a corkscrew morphology is interesting in its own right. While we are quick to emphasise that the scale of our simulation corresponds only to the very closest regions to the compact object, it is nevertheless noteworthy that the two closest examples of extragalactic jets, Centaurus A (Clarke, Burns, & Feigelson 1986) and M87 (Biretta, Zhou & Owen 1995) show definite side-to-side oscillations and/or helical morphologies in their structures. This behaviour is even clearer in the observations of wiggling optical jets from YSOs such as HH47 (Heathcote et al. 1996) and GGD 34 (Gomez de Castro & Robles 1999).

These jets are observed in optical forbidden lines, typically SII. As noted by Heathcote et al. (1996), supersonic jets tend to move ballistically making bending difficult to achieve. We note however that the relevant quantity that constrains the behaviour of magnetised flows is their Alfvén Mach number, which our simulations show adjust to near unity. Our simulations occur on scales that are about a decade smaller than the HST can resolve for nearby protostars. Nonetheless, the fact that some of our jet simulations settle into a wobbling or corkscrew configuration probably says something interesting about the larger scale behaviour as well.

Finally, we have seen that our simulated jets regain a reasonably stable configuration at late times. Indeed, various physical quantities in the jet, such as the strength of the toroidal field, the jet Mach number, etc., are rather close to their values at earlier times, before the unstable flute modes make their appearance (e.g., at $t \leq 50$). This strongly suggests that the jet would ultimately undergo another burst of unstable behaviour after it accelerates material to sufficiently high Alfvénic Mach number. Testing this conjecture requires a much larger simulation wherein one doubles or triples the size of the box to ensure that most of the body of the jet stays in the computational domain. It seems clear however, that the jet will undergo this kind of episodic behaviour, which in turns has interesting consequences for the appearance of multiple bow-shocks and other episodic phenomena that are seen in real jets.

R.O. thanks Axel Brandenburg, Wolfgang Dobler, Åke Nordlund, Anvar Shukurov, and Michel Tagger for helpful discussions. R.O. is supported by the Nordic Institute for Theoretical Physics (NORDITA). D.A.C. thanks Guy Pelletier and Pierre-Yves Longaretti for their gracious hospitality at l’Observatoire de Grenoble, during a sabbatical leave when much of this work was completed. The research of D.A.C. is supported by grants from the Natural Science and Engineering Research Council of Canada (NSERC), the Canada Foundation for Innovation (CFI) and the Atlantic Canada Opportunities Agency (ACOA). R.E.P. thanks Roger Blandford and Anneila Sargent for hospitality extended to him on a research leave at Caltech, where some of this work was completed, as well as Roger Blandford and Ruben Krasnopolsky for stimulating discussions on these topics. The research of R.E.P. is supported by an operating grant from NSERC.

A. BOUNDARY CONDITIONS

A.1. Truncating the Keplerian profile

A Keplerian profile,

$$v_K(r) = \frac{1}{\sqrt{r}} \tag{A.1}$$

is impractical to implement over all r on a numerical, Cartesian grid. In particular, the singularity at $r = 0$ must be avoided, and at the outer limits of the grid, due attention must be paid to the rotation in the grid “corners”.

The singularity can be handled most conveniently by setting $v_\phi(r) = 0$ for $r < r_i$. This solution, depicted in Fig. 2, results in a cusp at $r = r_i$, which may introduce numerical concerns of its own. Alternatively, one may introduce a transition region over which the Keplerian profile is continuously and smoothly connected to the $v_\phi(r) = 0$ solution inside r_i , also shown in Fig. 2. Both options were used in the simulations discussed in this paper, and the mathematical form of the smoothing function used is given below [equation (A.2)].

As for the outer regions of the grid, consider the corner of the computational domain in the $(+x, +y)$ quadrant, as depicted in Fig. 21. Here, two outflow boundaries meet, namely the $+x$ -boundary and the $+y$ -boundary. If rotation about the z -axis is positive (in the sense of the right-hand rule), then near the $(+x, +y)$ corner, the sense of rotation causes material to flow *out* across the $+y$ -boundary, which as an outflow boundary it can handle. On the same token, material should flow *in* through the $+x$ -boundary, which as an outflow boundary, cannot happen. Thus, a vacuum is created in the corners, adversely affecting the rest of the computational domain within a sound-crossing time.

For many reasons, it is impractical to suggest that the $+x$ boundary be redesignated as an inflow boundary. This would break the symmetry that must exist between the $+x$ - and $+y$ -boundaries, and would require inflow values to be specified *a priori* all along the $+x$ -boundary, which is not possible without the full time-dependent solution to the problem!

This problem doesn’t exist in cylindrical coordinates, of course, since there are no corners. We therefore try to mimic this desirable property of cylindrical coordinates by truncating the $v_\phi(r)$ profile at an “outer radius” r_o , where r_o is the radius of a cylinder which completely contains the primary computational domain, yet lies well inside the greater computational domain (Table 1, and Fig. 21). Thus, if there is no rotation in the corners, the problem of evacuating the corner regions is avoided.

If the truncation at r_o is sudden, then the outer boundary of the rotating cylinder will be ragged (being resolved on a Cartesian grid). This will create a large and undesirable

numerical viscosity along the outer surface of the cylinder, which can be largely avoided if we use a smooth truncation instead. Thus, we impose a continuous and smooth profile for $v_\phi(r)$ between r_o and r_{\max} , where $r_{\max} > r_o$ but still less than the maximum value along the x - and y -axes (for simulations A, B, C, and E, we used $r_o = 22$ and $r_{\max} = 28$, while for simulation D, we used $r_o = 30$ and $r_{\max} = 38$).

Therefore, the form of the azimuthal velocity profile, $v_\phi(r)$, used in these simulations which truncates the Keplerian profile [equation (A.1)] at both the inner and outer regions of the grid is given by:

$$v_\phi(r) = \begin{cases} 0 & r < r_1, \\ r^{-1/2} \sin^2\left(\frac{\pi}{2} \frac{r - r_1}{r_2 - r_1}\right) & r_1 \leq r < r_2, \\ r^{-1/2} & r_2 \leq r < r_o, \\ r^{-1/2} \cos^2\left(\frac{\pi}{2} \frac{r - r_o}{r_{\max} - r_o}\right) & r_o \leq r < r_{\max}, \\ 0 & r \geq r_{\max}, \end{cases} \quad (\text{A.2})$$

where all variables are scaled as described in §2.1. For simulations A–D, $r_1 = r_2 = r_i$, and there is no region in which the \sin^2 smoothing function is applied. For simulation E, $r_1 = \frac{1}{2}r_i$ and $r_2 = 2r_i$ and the \sin^2 solution raises the profile smoothly from 0 to the Keplerian value. For all simulations, the \cos^2 function allows the profile to drop off smoothly between r_o and r_{\max} , arriving at the minimum value (0) with zero slope.

Of course, once flow has advanced onto the grid by a few zones, the dynamics of the flow will have altered the velocity field significantly from whatever was specified at the boundary. Thus, which functions are used to smooth the profiles should not be critical.

A.2. Breaking the quadrantal symmetry

When attempting to break a geometric symmetry, experience has shown that it is preferable to impose perturbations to the velocity fields, rather than directly to the pressure or density distributions. Pressure perturbations send sound waves in all directions, which in a highly dynamic situation, can steepen into shocks and affect outlying regions more than the original perturbations may have intended.

Thus, we break the imposed quadrantal symmetry by introducing a non-azimuthal component to the velocity profile of the disc. We do this in two ways. The first, and perhaps most obvious way, is to offset the point about which the velocity profile in (A.2) is evaluated from the centre of the gravitational potential well. Then at some prescribed time, t_j , later,

the origin for the velocity profile is “jerked” to another location. This is implemented by replacing $r = \sqrt{x^2 + y^2}$ in equation (A.2) with ξ , where ξ is given by:

$$\xi = \begin{cases} \sqrt{(x - \delta r)^2 + y^2} & t < t_j, \\ \sqrt{x^2 - (y - \delta r)^2} & t > t_j, \end{cases} \quad (\text{A.3})$$

where δr is a few or a few tens of percent of r_i (it does not seem to matter), and where we used $t_j = 10$ (in scaled time units described in §2.1), though again, the precise time the origin is “jerked” does not matter. Simulations B and E were “jerked” in this manner to break the quadrantal symmetry.

For simulations C and D, the disc was “wobbled” by introducing a time-dependent radial component to the disc velocity profile. Thus, we use a disc velocity of the form:

$$\vec{v} = v_r(r, \phi, t) \hat{r} + v_\phi(r) \hat{\phi} \quad (\text{A.4})$$

where $v_\phi(r)$ is given by equation (A.2), and where the radial component, $v_r(r, \phi, t)$, is the perturbation and is given by

$$v_r(r, \phi, t) = \frac{\epsilon}{r} \cos(\phi + \omega t). \quad (\text{A.5})$$

As usual, the azimuthal coordinate, ϕ , is taken counter-clockwise from the $+x$ -axis, where the z -axis is the disc axis. We used $\epsilon = 0.02$ (a 2% perturbation at $r = r_i = 1$), and $\omega = 0.1$ (one tenth the Keplerian angular velocity at $r = r_i = 1$). The introduction of the radial velocity component distorts the otherwise circular velocity profile imposed by $v_\phi(r)$ alone into a precessing elliptical profile, with the origin of the gravitational potential located at the centre of the ellipse. The precession is introduced by virtue of the explicit time-dependence in (A.5), without which, the velocity profile would still possess quadrantal (though not azimuthal) symmetry.

We close this section by noting that “jerked” and “wobbling” the disc seems to give qualitatively identical results. Thus, how one chooses to break the quadrantal symmetry is a matter of taste, so long as the symmetry is truly broken.

A.3. Enforcing $\nabla \cdot \mathbf{v} = 0$ at the disc

Another consequence of using Cartesian coordinates is the numerical introduction of a divergence in what analytically is a solenoidal vector field. Physically, the velocity profile given by equation (A.4) is solenoidal at any given instant of time. This may be verified

by noting that the velocity streamlines form closed loops, or by evaluating the divergence directly.

However, as the disc is resolved on a Cartesian grid, the x - and y -components of \vec{v} must be evaluated, and if this is done by direct coordinate transformation (e.g., $v_x = v_r \cos \phi - v_\phi \sin \phi$, etc.), numerical truncation errors can generate significant non-zero divergences in a time short compared to the duration of the simulation.

First, we establish the need to preserve the solenoidal nature of the velocity profile to within machine roundoff errors, and then we show how this can be done. Consider the task of preserving B_z to a constant value on the surface of the disc, as required by these simulations. From the induction equation, we have

$$\frac{\partial B_z}{\partial t} = \frac{\partial \varepsilon_y}{\partial x} - \frac{\partial \varepsilon_x}{\partial y}, \quad (\text{A.6})$$

with ε_x and ε_y being the x - and y -components of the so-called e.m.f. (Evans & Hawley 1988), defined as $\vec{\varepsilon} = \vec{v} \times \vec{B}$. Thus, for $v_z = 0$,

$$\varepsilon_x = v_y B_z - v_z B_y = v_y B_z, \quad (\text{A.7})$$

$$\varepsilon_y = v_z B_x - v_x B_z = -v_x B_z \quad (\text{A.8})$$

For B_z to stay constant on the disc surface, equations (A.6), (A.7), and (A.8) require that

$$\left. \frac{\partial B_z}{\partial t} \right|_{z=0} = -B_z \left(\left. \frac{\partial v_x}{\partial x} + \frac{\partial v_y}{\partial y} \right) \right|_{z=0} = -B_z \nabla \cdot \vec{v} \Big|_{z=0} = 0, \quad (\text{A.9})$$

Thus, if $\nabla \cdot \vec{v} \neq 0$ to machine round-off errors (as would be the case if one naïvely evaluates v_x and v_y from the components of \vec{v}), B_z will evolve in time with profound and disastrous consequences. In our case, we noted that the growth of B_z was most severe near the inner boundary of the disc, causing the inner region of the atmosphere to be evacuated via numerically driven “jets”. With the Alfvén speed ($B/\sqrt{\rho}$) unbounded, the Alfvén time step vanished and the simulation ground to a halt.

The fix is simple, and recognisable by anyone who has faced the task of setting up a numerically solenoidal magnetic field. Consider the vector quantity \vec{q} given by $\vec{v} = \nabla \times \vec{q}$. Note that \vec{q} is to the velocity field what the vector potential is to the magnetic field. In cylindrical coordinates, if $\vec{v} = v_r \hat{r} + v_\phi \hat{\phi}$ [e.g., equation (A.4)], then $\vec{q} = q_z \hat{z}$, and;

$$v_r = \frac{1}{r} \frac{\partial q_z}{\partial \phi}; \quad v_\phi = -\frac{\partial q_z}{\partial r}. \quad (\text{A.10})$$

For the purposes of finding \vec{q} , let us assume that q_z is separable. Thus, let $q_z(r, \phi) = R(r) + \Phi(\phi)$. Then, inverting equations (A.10), we get

$$R(r) = - \int_{r_i}^r v_\phi(r') dr' \quad (\text{A.11})$$

and

$$\Phi(\phi) = \int_0^\phi v_r(\phi') d\phi' \quad (\text{A.12})$$

where v_ϕ is given by equation (A.2) and v_r is given by equation (A.5). Some of the cases in equation (A.2) are integrable analytically, and some require numerical integration. Regardless, for any given value of r , one can find $R(r)$ from equation (A.11). Meanwhile, v_r integrates trivially, giving

$$q_z = R(r) + \epsilon [\sin(\phi + \omega t) - \sin(\omega t)] \quad (\text{A.13})$$

Now, the z -components of vectors are invariant under the transformation between cylindrical and Cartesian coordinates. Thus, we may consider equation (A.13) to give the z -component of \vec{q} in Cartesian coordinates, and evaluate the x - and y -components of the truncated, perturbed Keplerian velocity profile from q_z . Thus;

$$v_x = \frac{\partial q_z}{\partial y}; \quad v_y = -\frac{\partial q_z}{\partial x} \quad (\text{A.14})$$

In particular, for a staggered mesh such as that employed by the ZEUS family of codes (Clarke, 1996), q_z as a quantity would be centred on the zone-edges parallel to the z -axis (Fig. 22). Thus, a y -difference of q_z centres v_x on the x -face (as required on the staggered mesh) while an x -difference of q_z centres v_y on the y -face (again, as required on the staggered mesh). Thus, the difference form of equations (A.14) is

$$v_x(i, j) = \frac{q_z(i, j+1) - q_z(i, j)}{\delta y(j)}, \quad (\text{A.15})$$

$$v_y(i, j) = -\frac{q_z(i+1, j) - q_z(i, j)}{\delta x(i)}, \quad (\text{A.16})$$

where we now write the variables as functions of their coordinate indices, (i, j) , rather than of the coordinates, (x, y) , themselves.

With the numerical divergence given by

$$\text{div}(\vec{v}) = \frac{v_x(i+1, j) - v_x(i, j)}{\delta x(i)} + \frac{v_y(i, j+1) - v_y(i, j)}{\delta y(j)}, \quad (\text{A.17})$$

it is left as a straight-forward exercise to show that the numerical divergence of \vec{v} will be zero to within machine round-off errors. Further, when averaged to the zone centres and combined quadratically, the velocity component in equations (A.15) and (A.16) reproduce the original velocity profile (equation A.4) to within a few percent, depending on the coarseness of the grid chosen.

A.4. Magnetic Outflow Conditions

To be frank, it is still unclear what the “optimal” magnetic outflow boundary conditions should be. In the ZEUS-2D simulations described in OPI and OPII, for example, both ε_ϕ (the only component of the e.m.f. tracked in ZEUS-2D, and used to update the poloidal components of the magnetic field), and B_ϕ are kept constant across outflow boundaries. Note that setting ε_ϕ constant across the boundary is not at all the same as setting the poloidal field components themselves constant across the same boundary. For example, if B_r is initialised everywhere to zero and ε_ϕ is set constant across outflow boundaries (as in OPII), B_r will forever remain zero outside a z -outflow boundary (because $\partial\varepsilon_\phi/\partial z$ remains zero across the boundary) even if B_r just inside the boundary were to become non-zero. On the other hand, if B_r were set constant across the outflow boundary, the value of B_r outside the z -boundary would change with the values just inside the grid.

Thus, the toroidal and poloidal magnetic field components are treated differently across an outflow boundary in ZEUS-2D, and yet there were no physical principles used to justify this (Jim Stone, private communication). Still, when one tries the obvious alternative of setting the poloidal components of the magnetic field constant across an outflow boundary, severe numerical errors occur at the boundary yielding an unphysical build-up of magnetic stresses which evacuate the boundary zones. The combination of large magnetic field and low density results in very high Alfvén speeds and thus vanishingly small Alfvén time steps, grinding the simulation to a halt.

Unfortunately, there is no obvious way to extend the *ad hoc* prescription for magnetic outflow boundary conditions used in 2-D cylindrical coordinates (namely, maintaining continuous B_ϕ and ε_ϕ across boundaries) to 3-D Cartesian coordinates. For the present, we set all magnetic field components constant across outflow boundaries, and then impose floor values on the density near the outflow boundary to prevent the Alfvén time step from vanishing. To avoid the bad densities and ensuing dynamics from corrupting the solution as soon as the outflow reaches the boundary, we have pushed the actual outflow boundary well away from the primary region of interest, and filled the intervening regions with increasingly coarse zones (Fig. 1, §3.2). Eventually, the effects of the magnetic stresses building up on the

distant outflow boundaries make their presence felt on the primary computational domain, and it is at this point that the simulation is stopped. While not an ideal solution, it is a practical one, without which, the simulations presented herein could not have been evolved as far as they were.

REFERENCES

- Appl, S. & Camenzind, M. 1992, A&A, 256, 354
- Bateman, G. 1980, MHD Instabilities (Cambridge: MIT Press)
- Begelman, M. C., Blandford, R. D., & Rees, M. 1984
- Biretta, J. A., Zhou, F. & Owen, F. N. 1995, ApJ, 447, 582
- Blandford, R. D. & Payne, D. R. 1982, MNRAS, 199, 883 (BP)
- Burrows, C. J. et al. ApJ, 473, 437
- Cao, X. & Spruit, H. C. 1994, A&A, 287, 80
- Clarke, D. A. 1996, ApJ, 457, 291
- Clarke, D. A., Burns, J. O., & Feigelson, E. D. 1986, ApJ, 300, L41
- Clarke, D. A., Norman, M. L., & Burns, J. O. 1986, ApJ, 311, L63
- Eichler, D. 1993, ApJ, 419, 111
- Evans, C. R. & Hawley, J. F. 1988, ApJ, 332, 659
- Ferrari, A., Trussoni, E., & Zaninetti, L. 1981, MNRAS, 196, 1051
- Ferreira, J. 1997, A&A, 319, 340
- Fiedler, R. & Jones, T. W. 1984, ApJ, 283, 532
- Gill, A. E. 1965, Phys. Fluids, 8, 1428
- Gomez De Castro, A. I. & Robles, A. 1999, A& A, 344, 632
- Hardee, P. E., Clarke, D. A. & Rosen, A. 1997, ApJ, 485, 533
- Hardee, P. E. & Rosen, A. 1999, ApJ, 524, 650

- Hawley, J. F. & Stone, J. M. 1995, *Comp. Phy. Commun.*, 89, 127
- Heathcote, S. et al., 1996, *AJ*, 112, 1141
- Heinemann, M. & Olbert, S. 1978, *JGR*, 83, 2457
- Jørgensen, M. A. S., Ouyed, R. & Christensen, M. 2001, *A&A*, 379, 1170
- Königl, A. & Pudritz, R. E, in *Protostars and Planets IV*, edited by V. Mannings, A. P. Boss, & S. S. Russell (Tucson: University of Arizona Press), 759.
- Krasnopolsky, R., Li, Z.-Y., & Blandford, R. D., *astro-ph/9902200* (KLB).
- Kudoh, T., Matsumoto, R., & Shibata, K. 1998, *ApJ*, 508, 186
- Lucek, S. G. & Bell, A. R. 1996, *MNRAS*, 281, 245
- Meier, D. L., Eddington, S., Godon, P., Payne, D. G., & Lind, K. R. 1997, *Nature*, 388, 350
- Mirabel, I. F. & Rodriguez, L. F. 1998, *Nature*, 392, 673
- Ostriker, E. 1997, *ApJ.*, 486, 291
- Ouyed, R. & Pudritz, R. E. 1997a, *ApJ*, 482, 712 (OPI).
- Ouyed, R. & Pudritz, R. E. 1997b, *ApJ*, 484, 794 (OPII).
- Ouyed, R. & Pudritz, R. E. 1999, *MNRAS*, 309, 233 (OPIII).
- Pelletier, G. & Pudritz, R. E. 1992, *ApJ*, 394, 117
- Pudritz, R. E. & Norman, C. 1983, *ApJ.*, 274, 677
- Pudritz, R. E. & Norman, C. 1986, *ApJ.*, 301, 501
- Ray, T. P. 1981, *MNRAS*, 196, 195
- Ray, T. P., et al. 1997, *Nature*, 385, 415
- Roberts, P. H. 1967, *Introduction to Magnetohydrodynamics*, (London: Longmans), p235
- Romanova, M. M., Ustyugova, G. V., Koldoba, A. V., Chechetkin, V. M., & Lovelace, R. V. 1997, *ApJ*, 482, 708
- Spruit, H. C., Foglizio, T., & Stehle, R. 1997, *MNRAS*, 288, 342
- Stone, J. M. & Norman, M. L. 1992a, *ApJS*, 80, 753

Stone, J. M. & Norman, M. L. 1992b, ApJS, 80, 791

Todo, Y. et al. 1993, ApJ, 403, 164

Ustyugova, G. V. et al., 1998, ApJ, 500, 703

van Leer, B. 1974, J. Comp. Phys., 23, 276

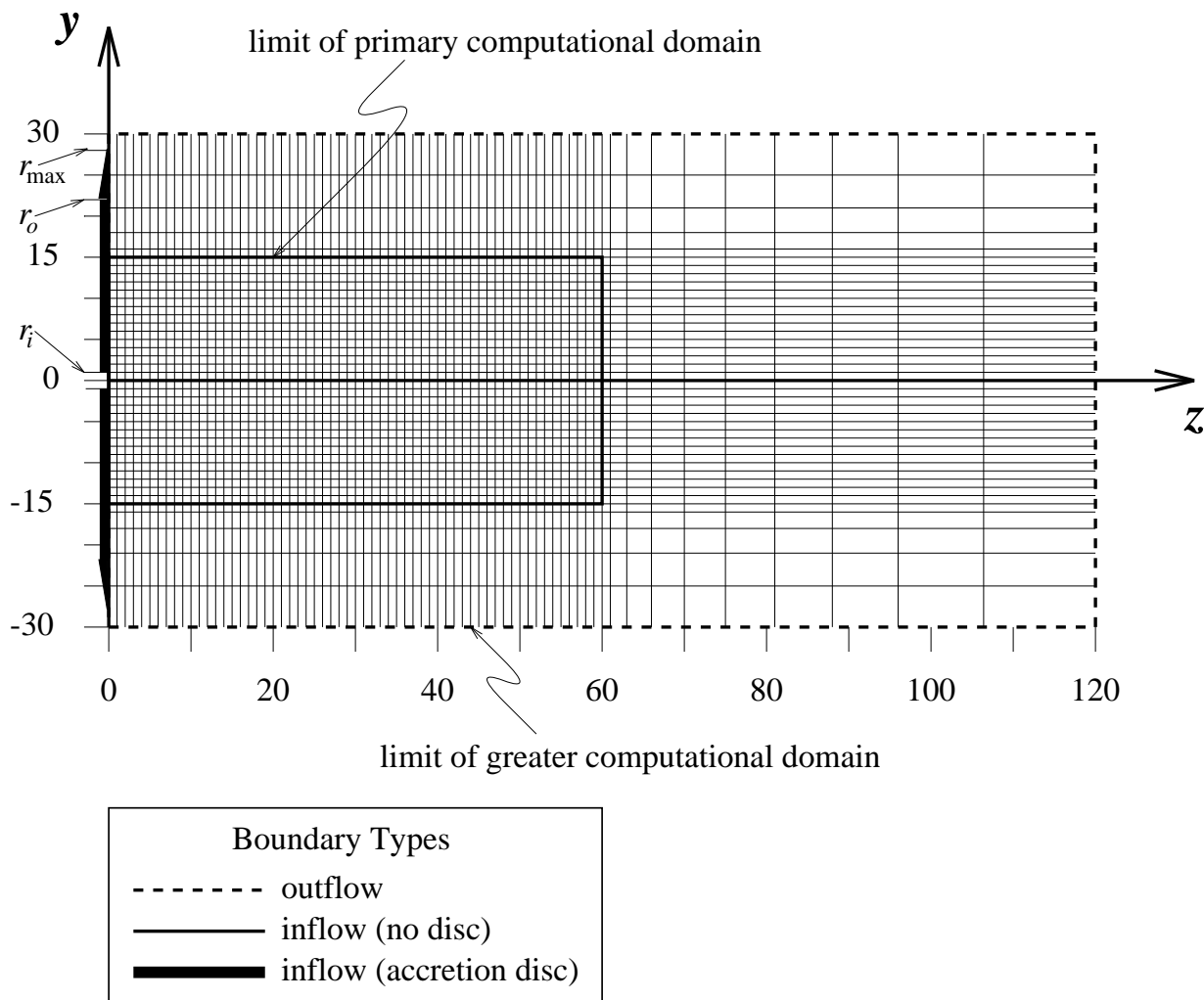


Fig. 1.— A schematic of the y - z slice of the 3-D grid for simulations A, B, C, and E that contains the disc (z) axis. The x -axis, which is zoned identically to the y -axis, points into the page at $z = y = 0$. Inflow conditions are imposed at the left boundary (y -axis) which includes the accretion disc between r_i and r_{\max} (designated by the heavy black line). All other boundaries (dashed) are designated as “outflow” boundaries. In this schematic, only every other zone is represented.

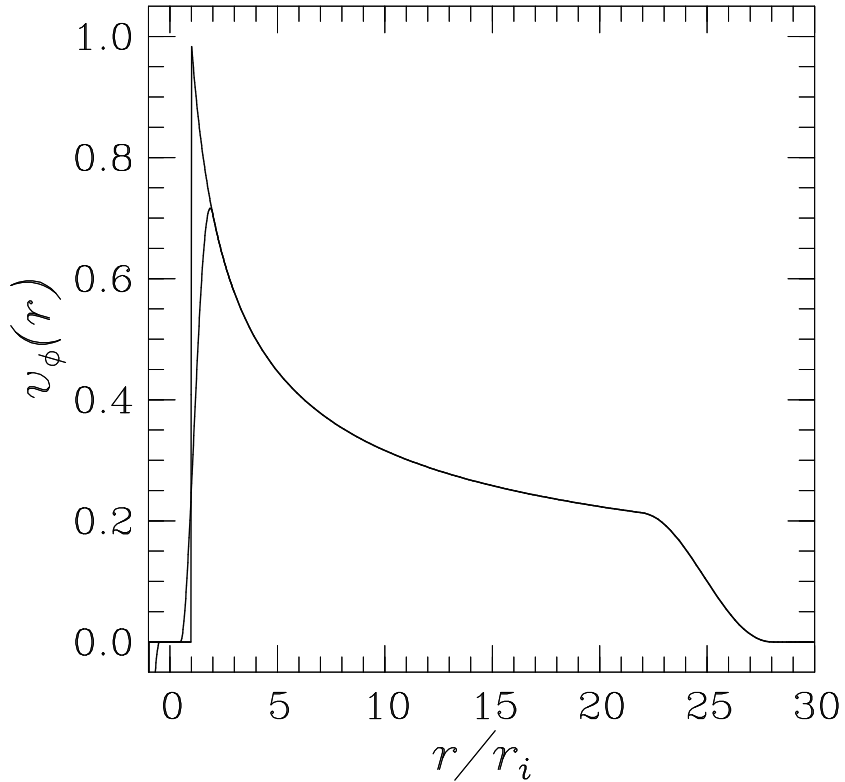


Fig. 2.— Profiles for $v_\phi(r)$ in the disc [given by equation (A.2) in Appendix A] for simulations A–C (cusp at $r = r_i$) and E (smoothed in the region $\frac{1}{2}r_i < r < 2r_i$). The $v_\phi(r)$ profile used in simulation D is the same as the cusped profile, except it extends to $r = 40r_i$, with the cutoff occurring between $30r_i < r < 38r_i$. The dramatic differences between simulations D and E can be largely attributed to the different profiles for $v_\phi(r)$.

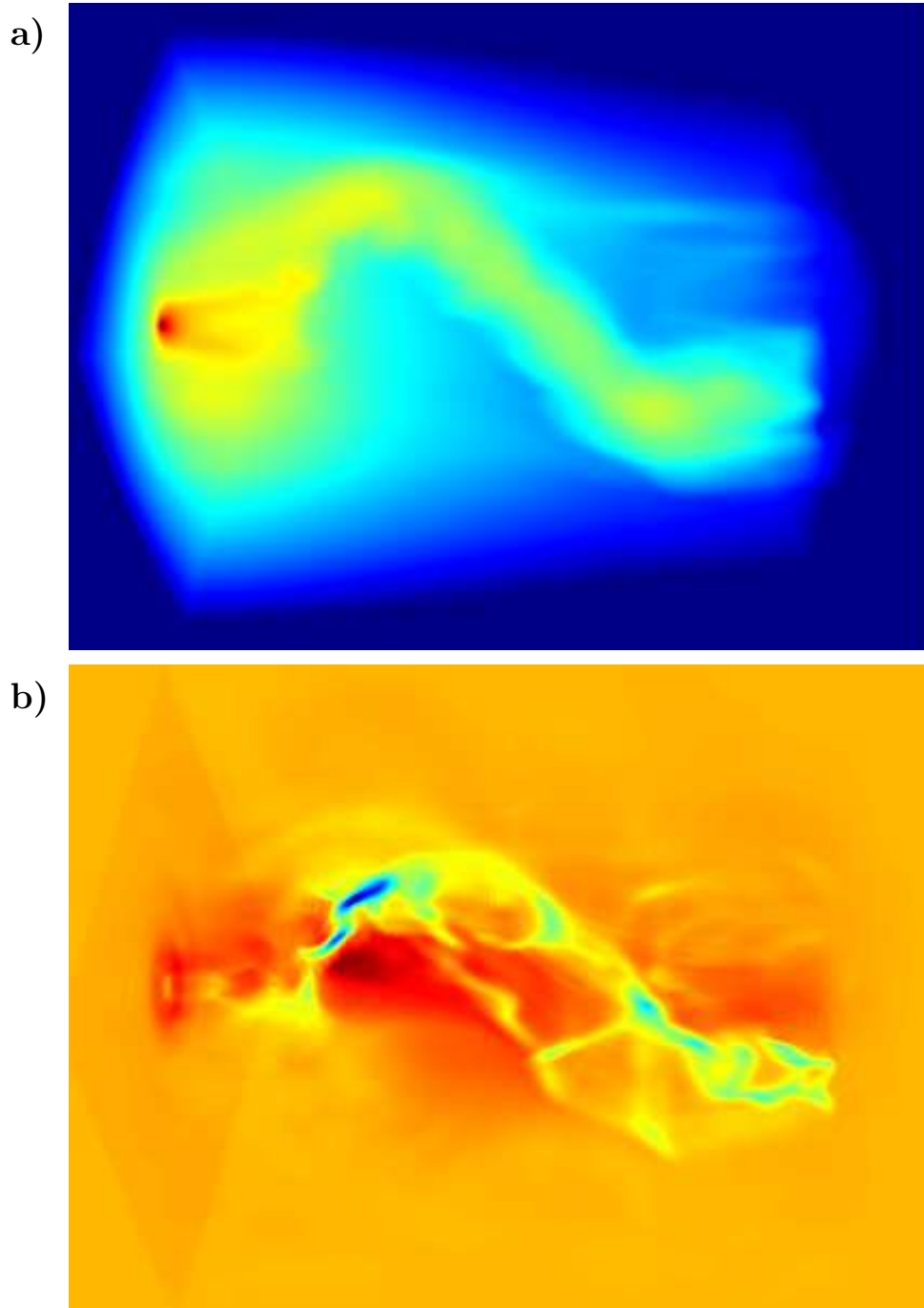


Fig. 3.— False colour representation of a) $\int \rho dl$ and b) $\int \nabla \cdot \vec{v} dl$ for simulation D. The disc is on the left side (not visible), and flow is generally from left to right. Colours are arranged spectrally from blue to red to represent low and high values of the variable.

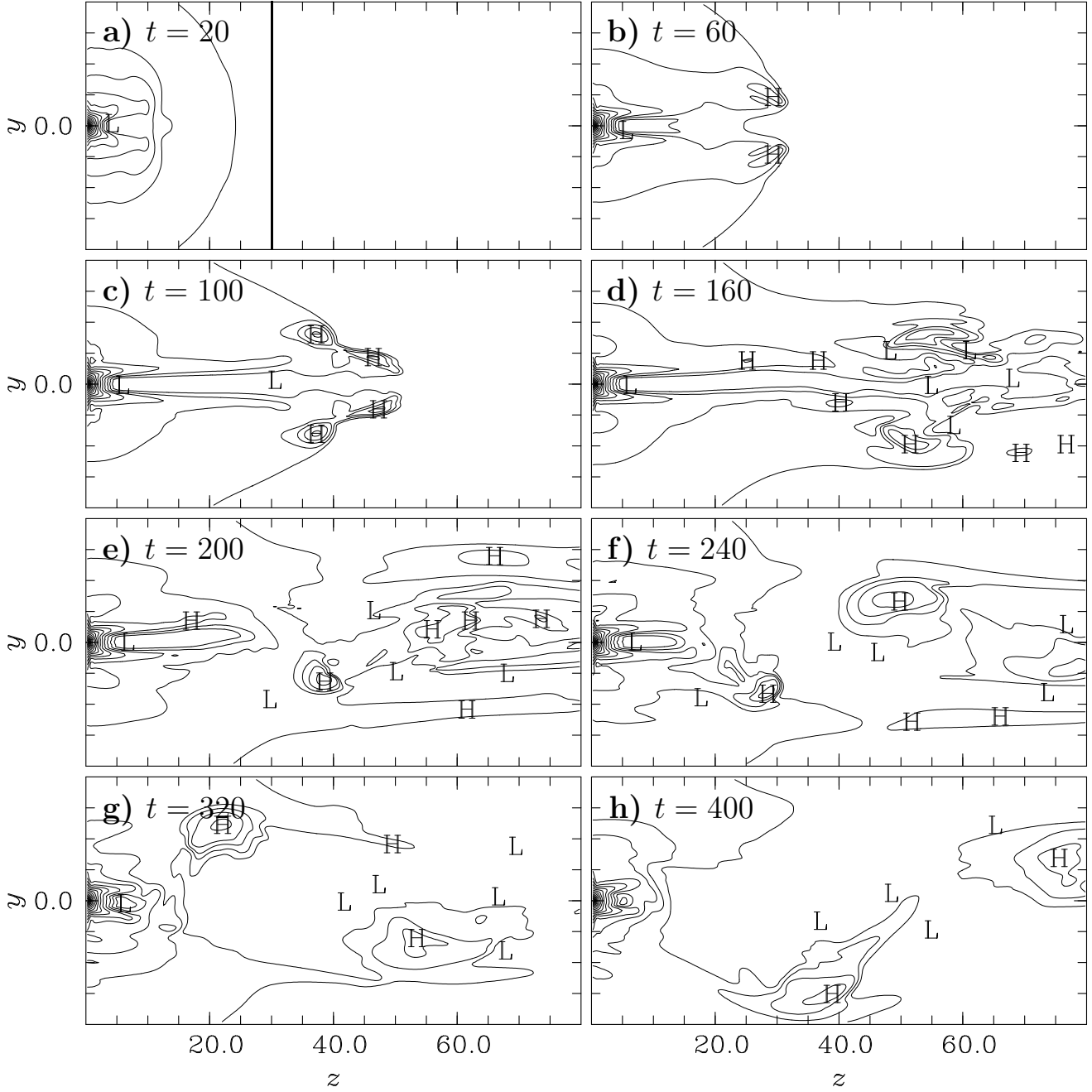


Fig. 4.— 2-D contour slices of the density on the y - z plane [where the z -axis (horizontal) is the disc axis] for simulation D shown at $t =$ a) 20, b) 60, c) 100, d) 160, e) 200, f) 240, g) 320, and h) 400. The $+x$ -axis, located at $y = z = 0$, points into the page. H and L indicate local maxima and minima respectively. The vertical line in panel a) (at $z = 30$) indicates the location of the cross-sectional slices in Figs. 7–10. The y -axis extends to ± 20 .

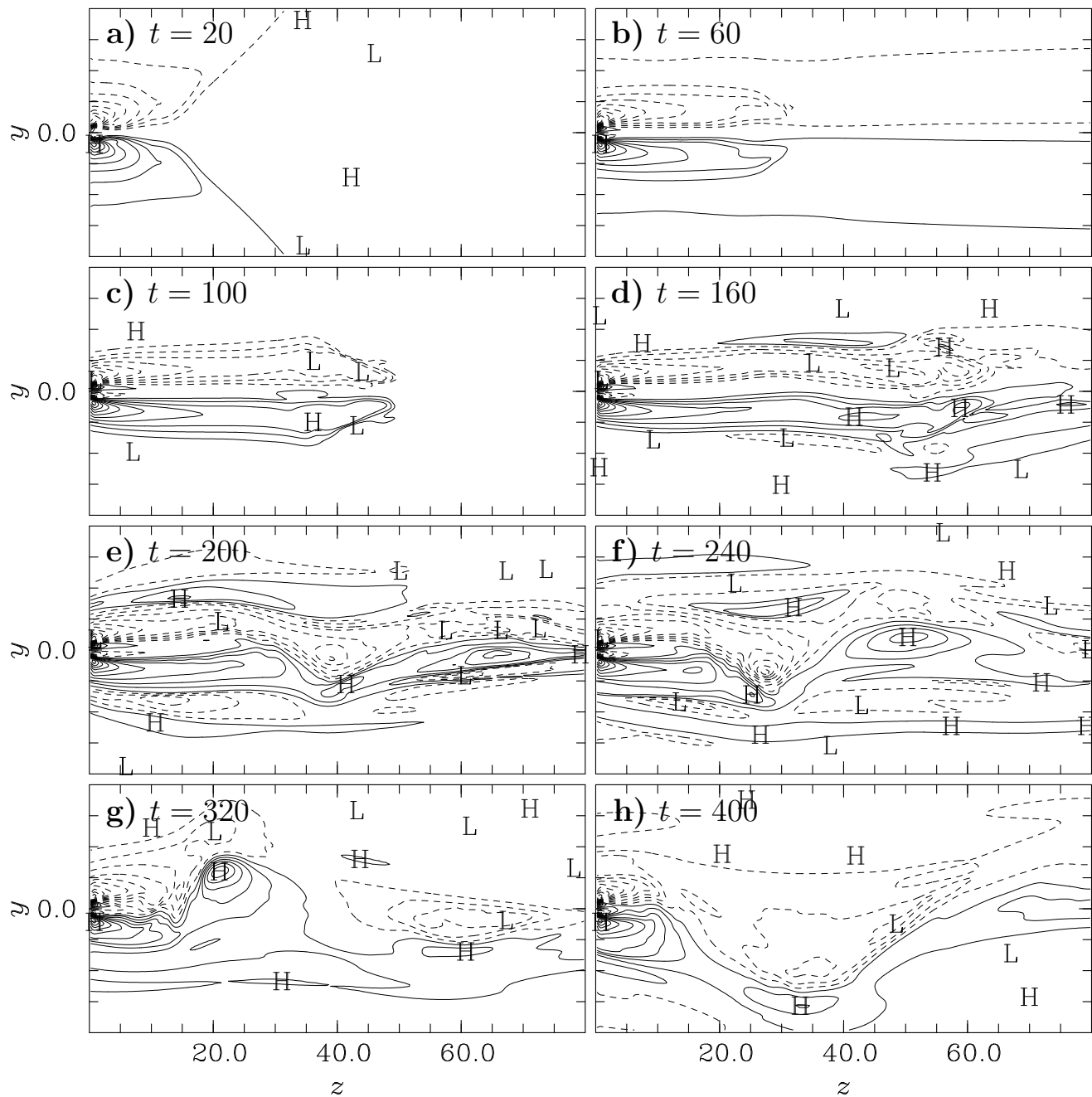


Fig. 5.— 2-D contour slices of the (toroidal) magnetic field component going into (dashed contours) or coming out of (solid contours) the page on the y - z plane [where the z -axis (horizontal) is the disc axis] for simulation D shown at the same times as Fig. 4. H and L indicate local maxima and minima, respectively. The y -axis extends to ± 20 .

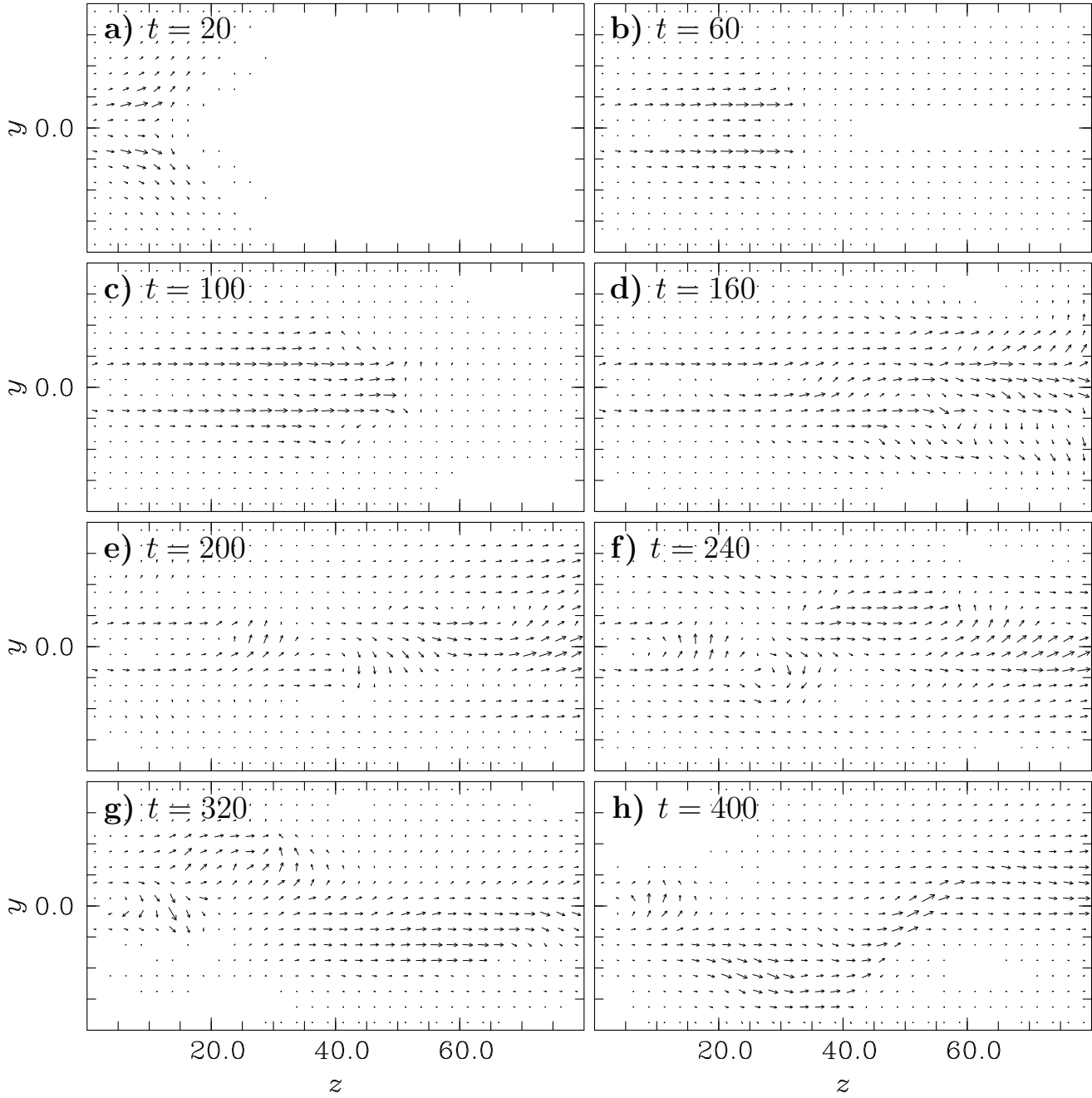


Fig. 6.— 2-D vector slices of the poloidal velocity components [within the y - z plane where the z -axis (horizontal) is the disc axis] for simulation D shown at the same times as Fig. 4. The y -axis extends to ± 20 .

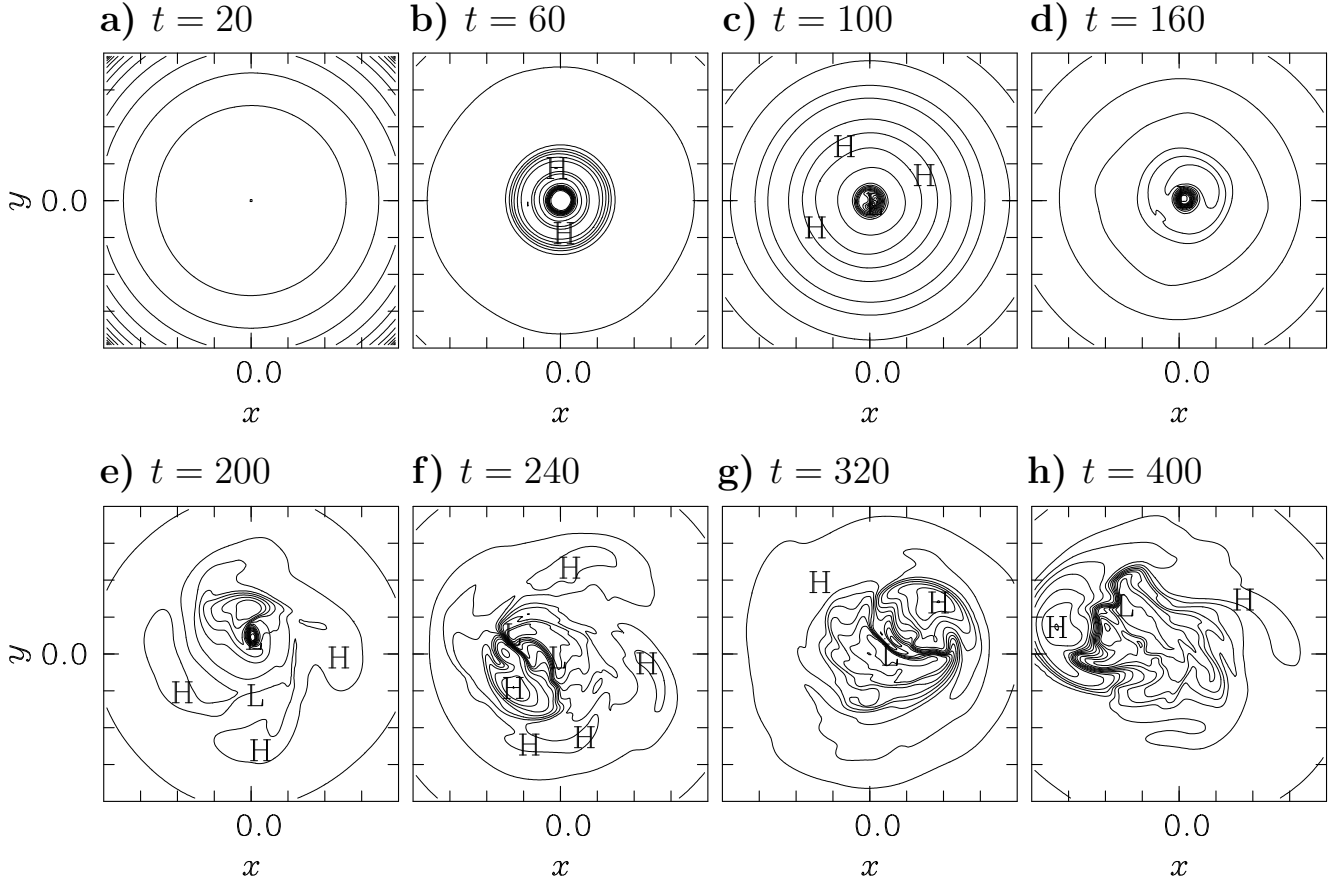


Fig. 7.— 2-D contour slices of density on the x - y plane at $z = 30$ (corresponding to the vertical line in Fig. 4a) for simulation D shown at the same times as Fig. 4. H and L indicate local maxima and minima respectively. The x and y axes extend to ± 20 (i.e., the entire primary computational domain). From this vantage, the z -axis points out of the page from the centre of each plot, and the sense of disc rotation is counter-clockwise. At early times, the circular contours reflect the initial spherically-symmetric atmosphere, but by $t = 200$ (panel e), the $m = 4$ mode arising from the quadrantal symmetry of the grid is apparent. At higher times, the $m = 4$ mode gives way to the $m = 1$ mode, forcing the jet axis well off the z -axis of the grid.

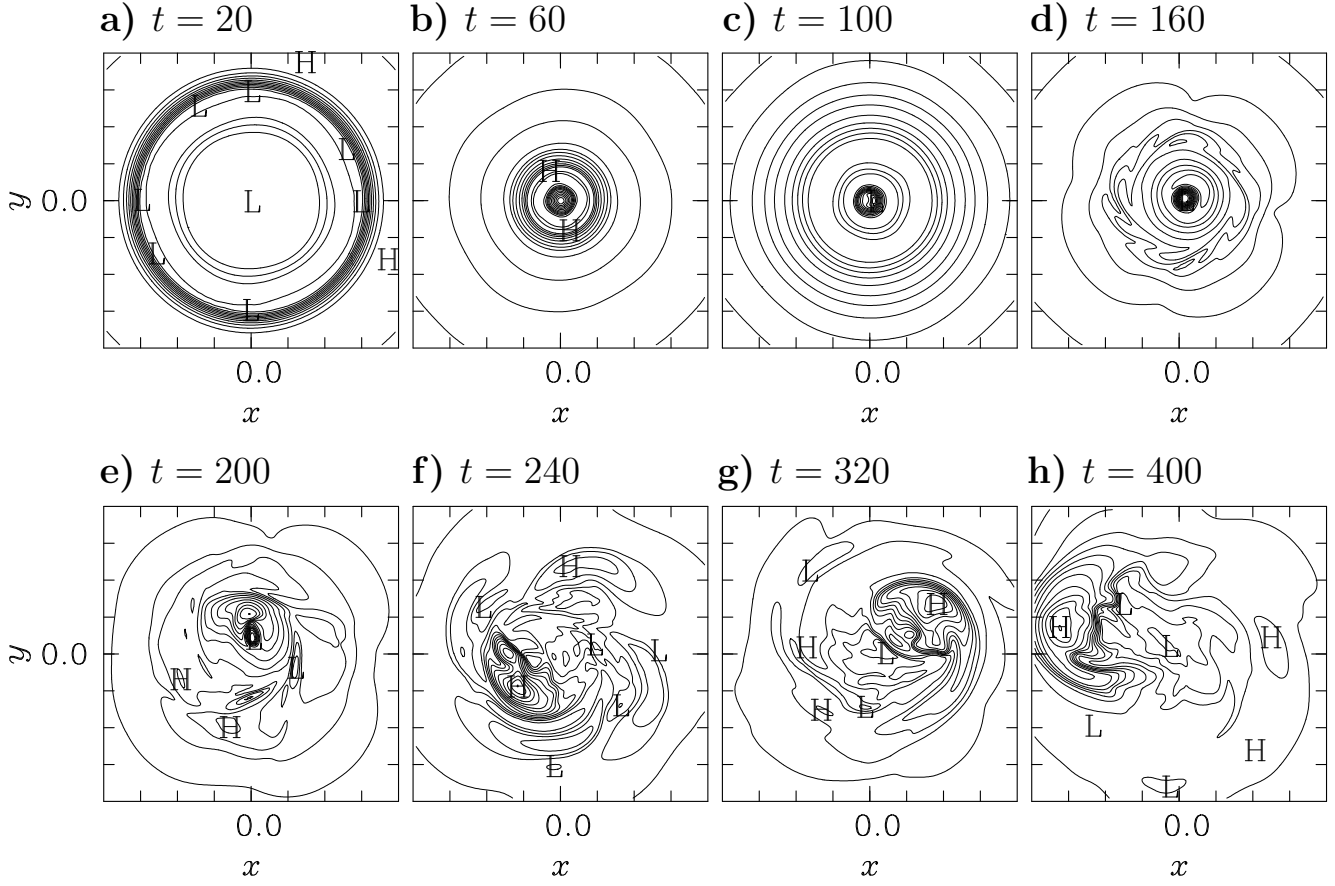


Fig. 8.— 2-D contour slices of the Alfvén Mach number (M_A) on the x - y plane at $z = 30$ for simulation D shown at the same times as Fig. 4. Particularly from $t = 200$ and on, the, maxima of M_A near the core of the jet correspond to the density maxima seen in Fig. 7.

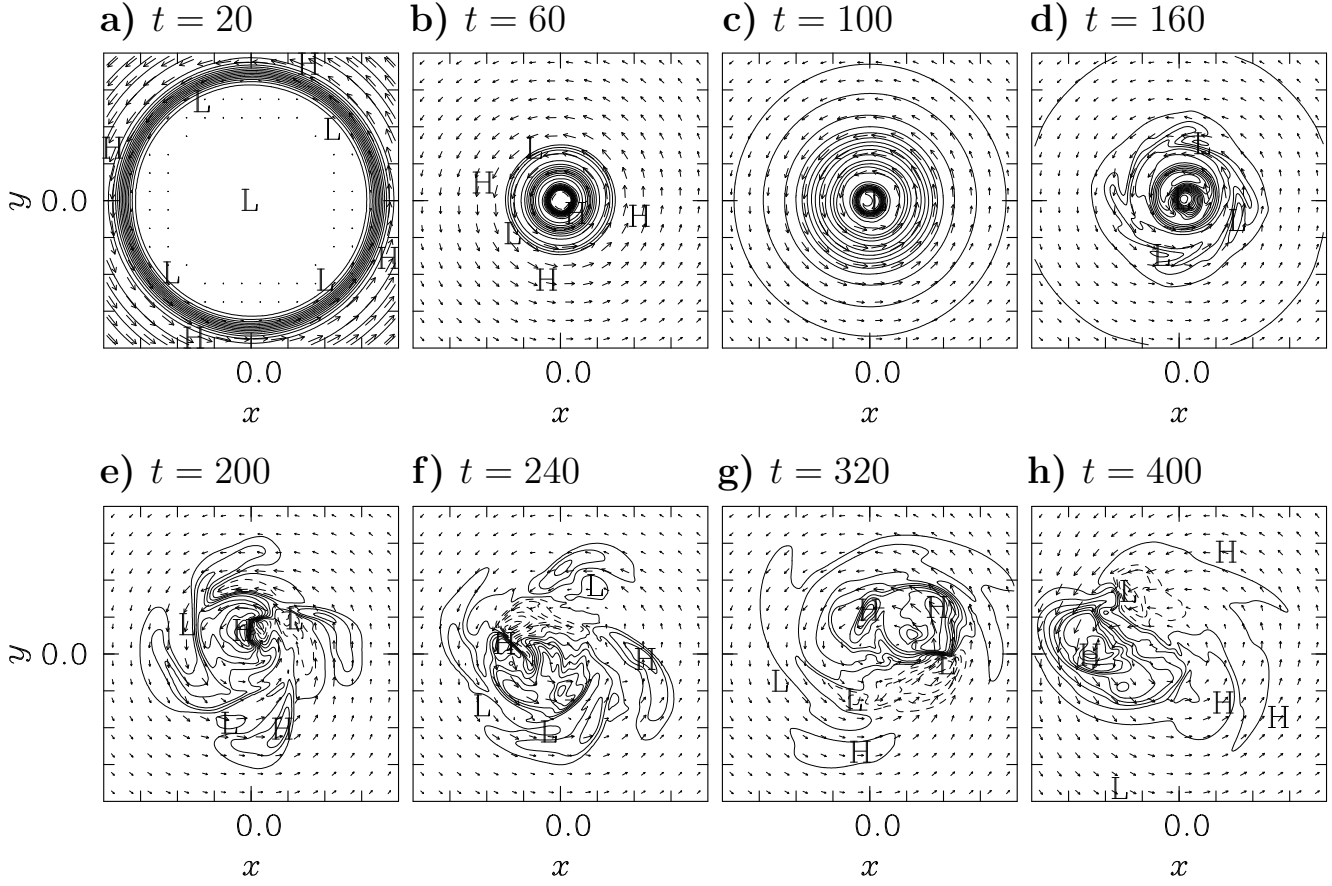


Fig. 9.— 2-D contour slices of the normal velocity (v_z) with poloidal velocity vectors ($v_x \hat{x} + v_y \hat{y}$) superimposed on the x - y plane at $z = 30$ for simulation D shown at the same times as Fig. 4. Dashed contour lines indicate flow into the page. Maximum normal velocities correspond to maxima in both density (Fig. 7) and normal magnetic field (Fig. 10).

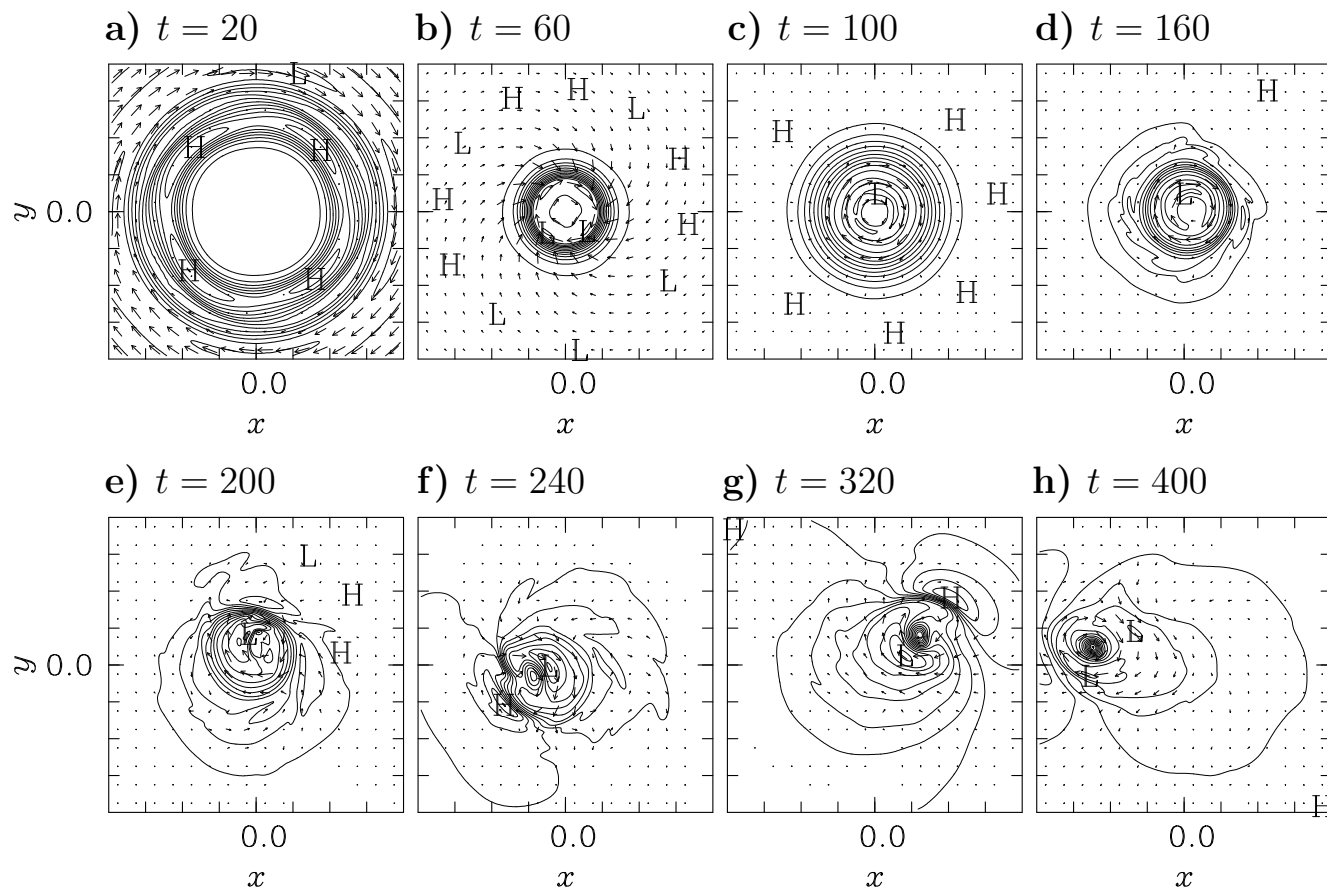


Fig. 10 .— 2-D contour slices of the normal magnetic field (B_z) with poloidal magnetic field vectors ($B_x \hat{x} + B_y \hat{y}$) superimposed on the x - y plane at $z = 30$ for simulation D shown at the same times as Fig. 4. At $t = 20$, the toroidal magnetic field wraps clockwise about the z -axis, as expected from the torsional Alfvén wave launched by the counter-clockwise rotation of the disc. At later times, a magnetic “spine” (compact circular feature in panels f, g, and h) develops. The density maxima (Figs. 7g and 7h) are offset from the spine away from the z -axis, as though the centre of mass of the jet is being driven centrifugally outwards from the magnetic spine by the rotation of the jet.

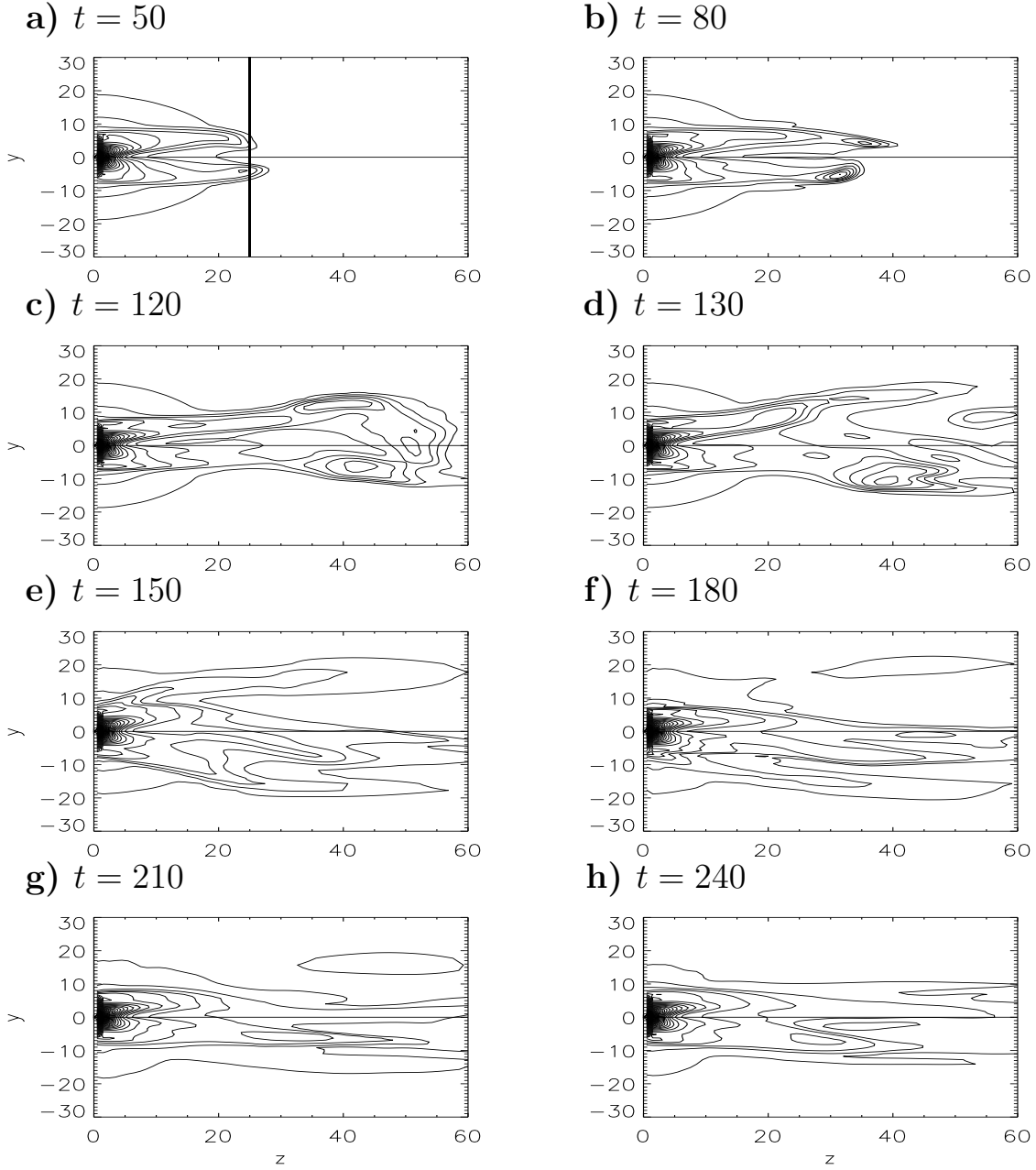


Fig. 11.— 2-D contour slices of density on the y - z plane [where the z -axis (horizontal) is the disc axis] for simulation E shown at $t =$ a) 50, b) 80, c) 120, d) 130, e) 150, f) 180, g) 210, and h) 240. The $+x$ -axis (located at $y = z = 0$) points into the page. The vertical line in panel a) (at $z = 25.0$) indicates the location of the cross-sectional slices in Figs. 13 and 17, and used to create Fig. 18.

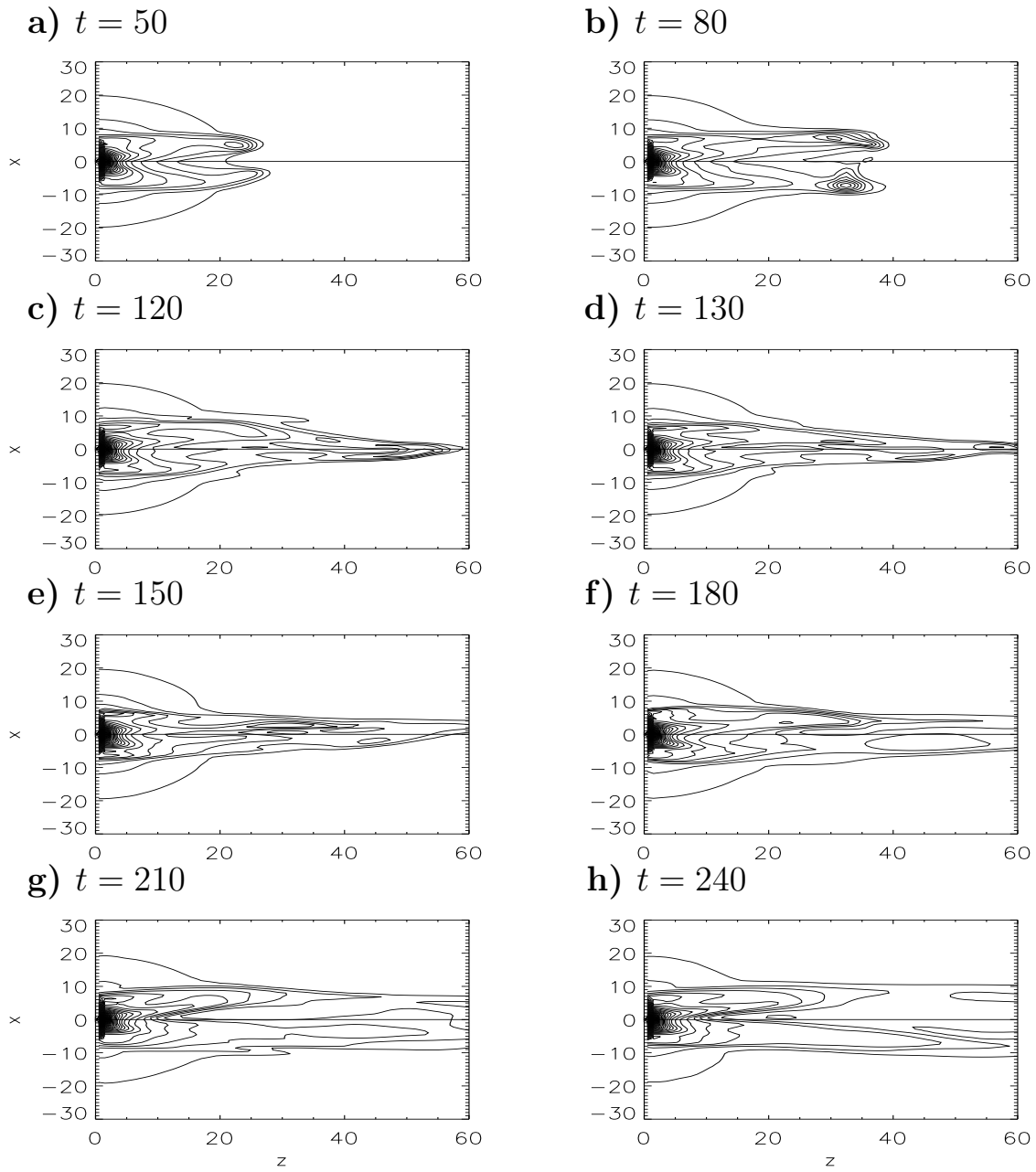


Fig. 12.— 2-D contour slices of density on the x - z plane [where the z -axis (horizontal) is the disc axis] for simulation E shown at $t =$ a) 50, b) 80, c) 120, d) 130, e) 150, f) 180, g) 210, and h) 240. The $+y$ -axis (located at $x = z = 0$) points into the page.

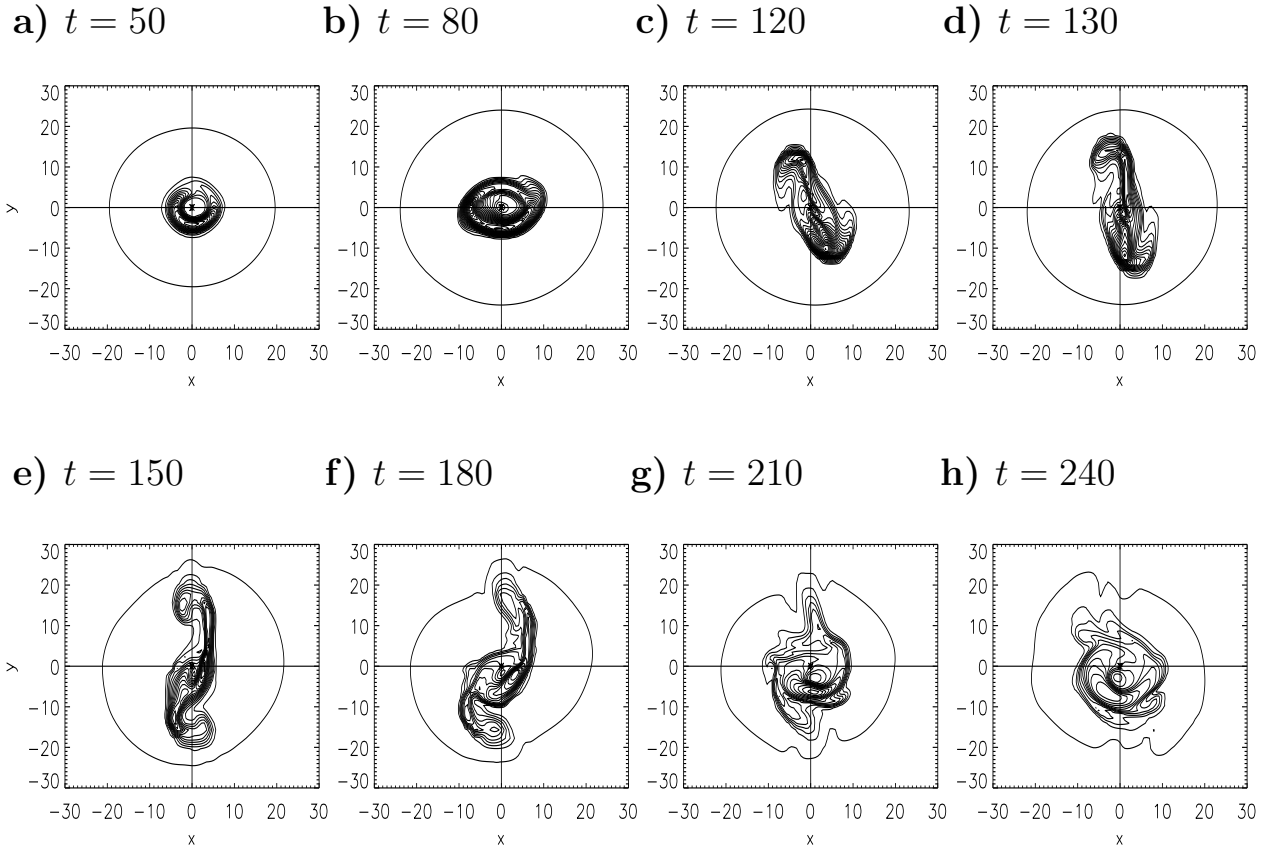
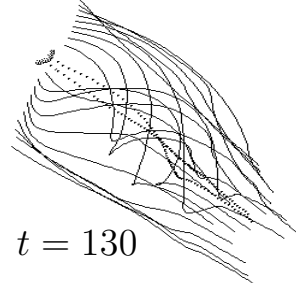
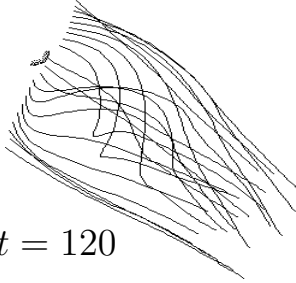


Fig. 13.— 2-D contour slices of density on the x - y plane at $z = 25.0$ (corresponding to the vertical line in Fig. 11a) for simulation E shown at the same times as Fig. 11.

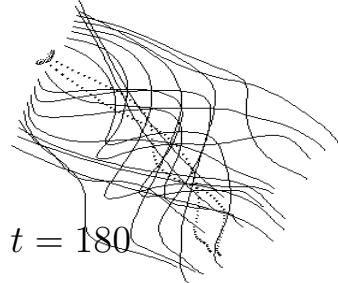
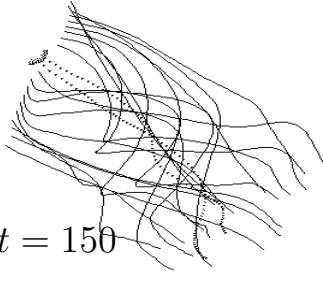
a) $t = 50$

b) $t = 80$



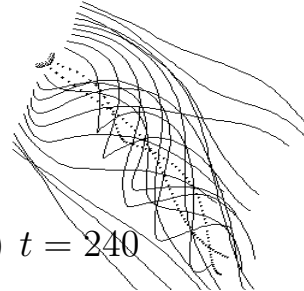
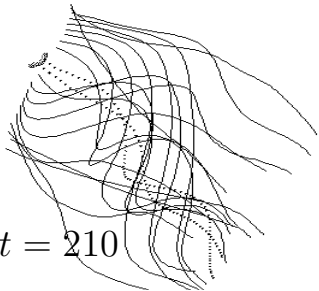
c) $t = 120$

d) $t = 130$



e) $t = 150$

f) $t = 180$



g) $t = 210$

h) $t = 240$

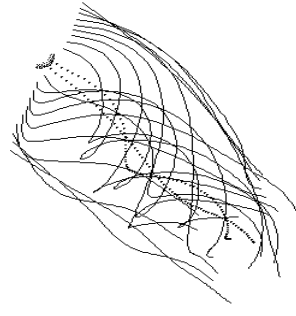
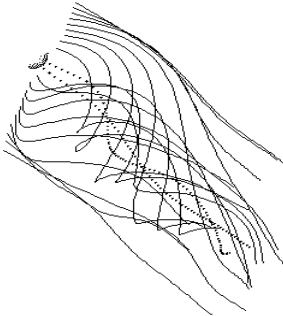
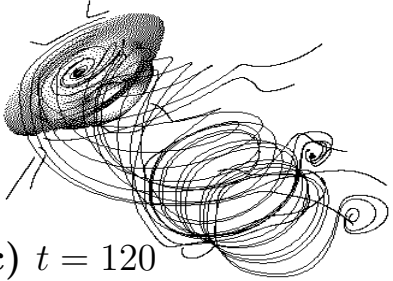
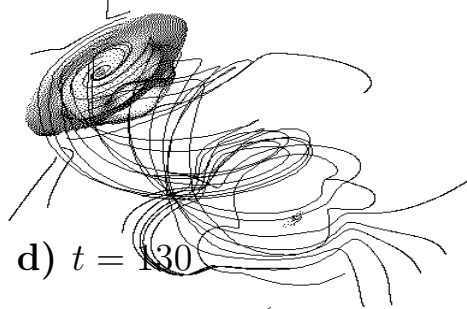


Fig. 14.— Snapshots of 20 magnetic field lines for simulation E shown at the same times as Fig. 11. The two central magnetic field lines (dotted lines) originate on the central compact object (illustrated by the semi-sphere to the left). They are not attached to the disk surface ($r < r_i$) and do not rotate. The disc axis is along the diagonal of the frame (on a 45° angle).

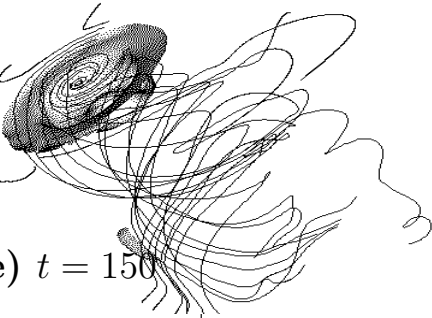
a) $t = 50$



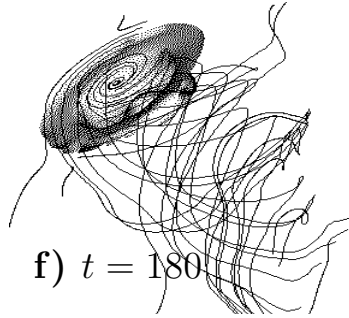
b) $t = 80$



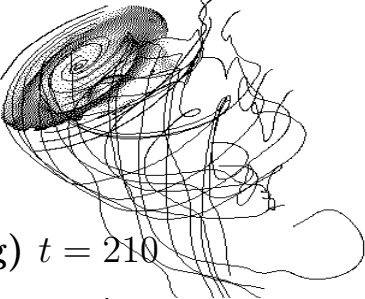
c) $t = 120$



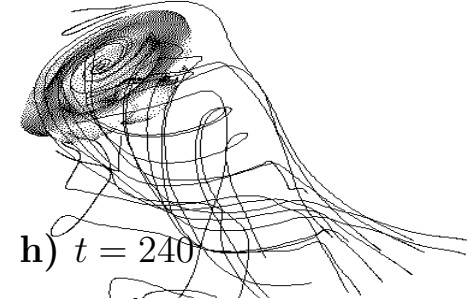
d) $t = 160$



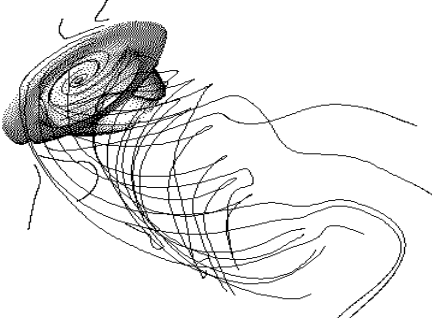
e) $t = 150$



f) $t = 180$



g) $t = 210$



h) $t = 240$

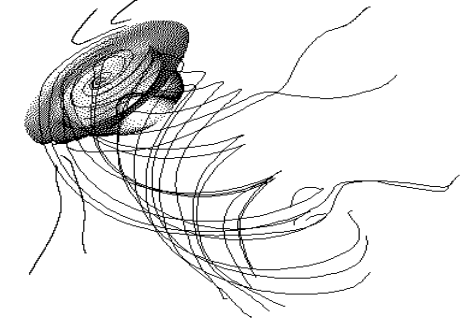
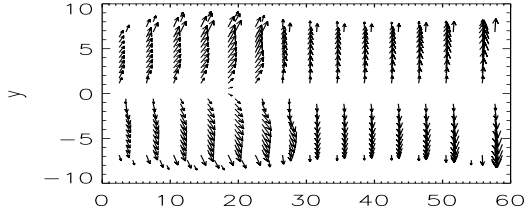
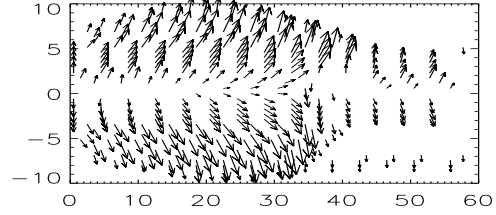


Fig. 15.— Snapshots of 20 streamlines for simulation E shown at the same times as Fig. 11 and with the same orientation as Fig. 14. The density isosurface is shown to illustrate the regions of high pressure. An appropriate density isosurface was chosen which best shows the section of the disk which participates in the outflow ($r \leq 5r_i$).

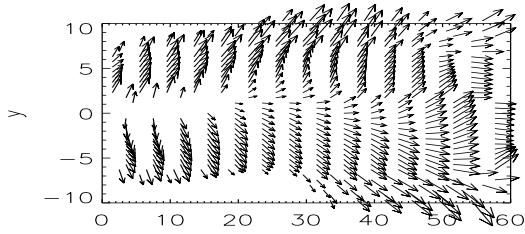
a) $t = 50$



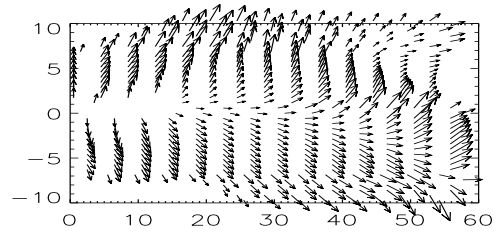
b) $t = 80$



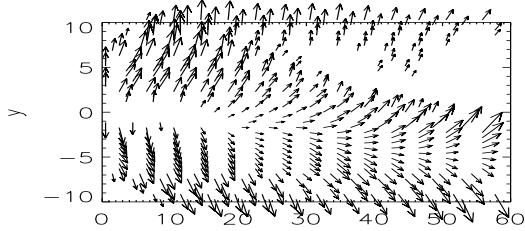
c) $t = 120$



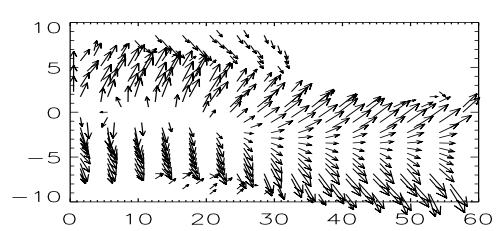
d) $t = 130$



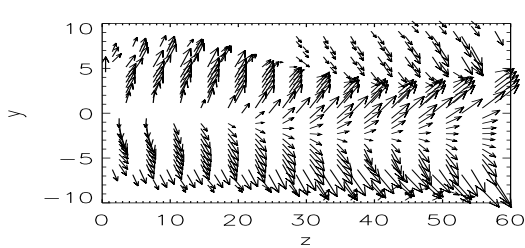
e) $t = 150$



f) $t = 180$



g) $t = 210$



h) $t = 240$

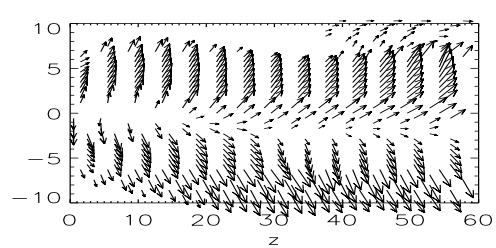


Fig. 16.— 2-D vector plots of poloidal velocity in the y - z plane [where the z -axis (horizontal) is the disc axis] for simulation E, shown at the same times as Fig. 11. Only the inner 2/3 of the plane [(y, z) = ($-10 : 10, 0 : 60$)] is shown. The maximum vector length is $0.5V_{K,i}$.

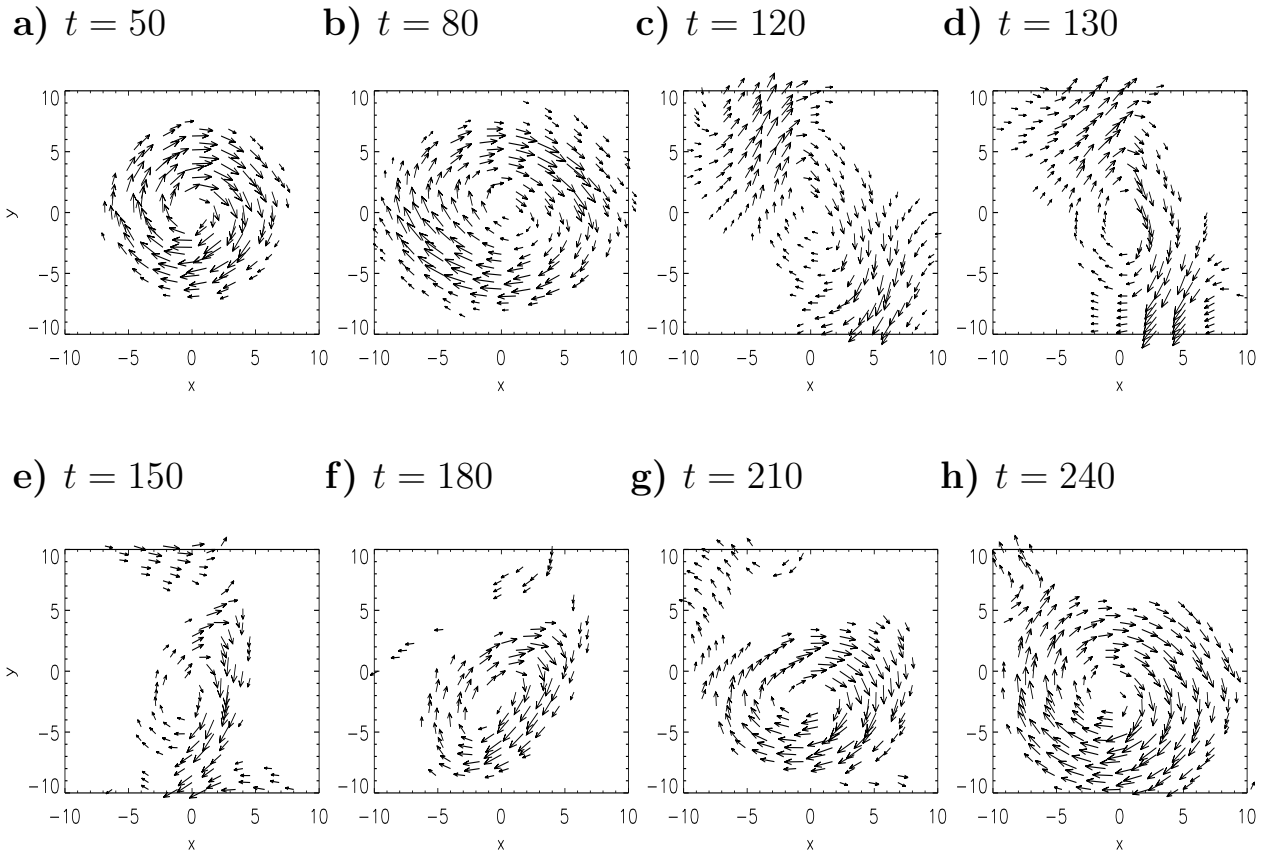


Fig. 17.— 2-D vector plots of poloidal velocity in the x - y plane at $z = 25.0$ for simulation E, shown at the same times as Fig. 11. Only the inner half of the plane $[(x, y) = (-10 : 10, -10 : 10)]$ is shown. The maximum vector length is $0.5V_{K,i}$

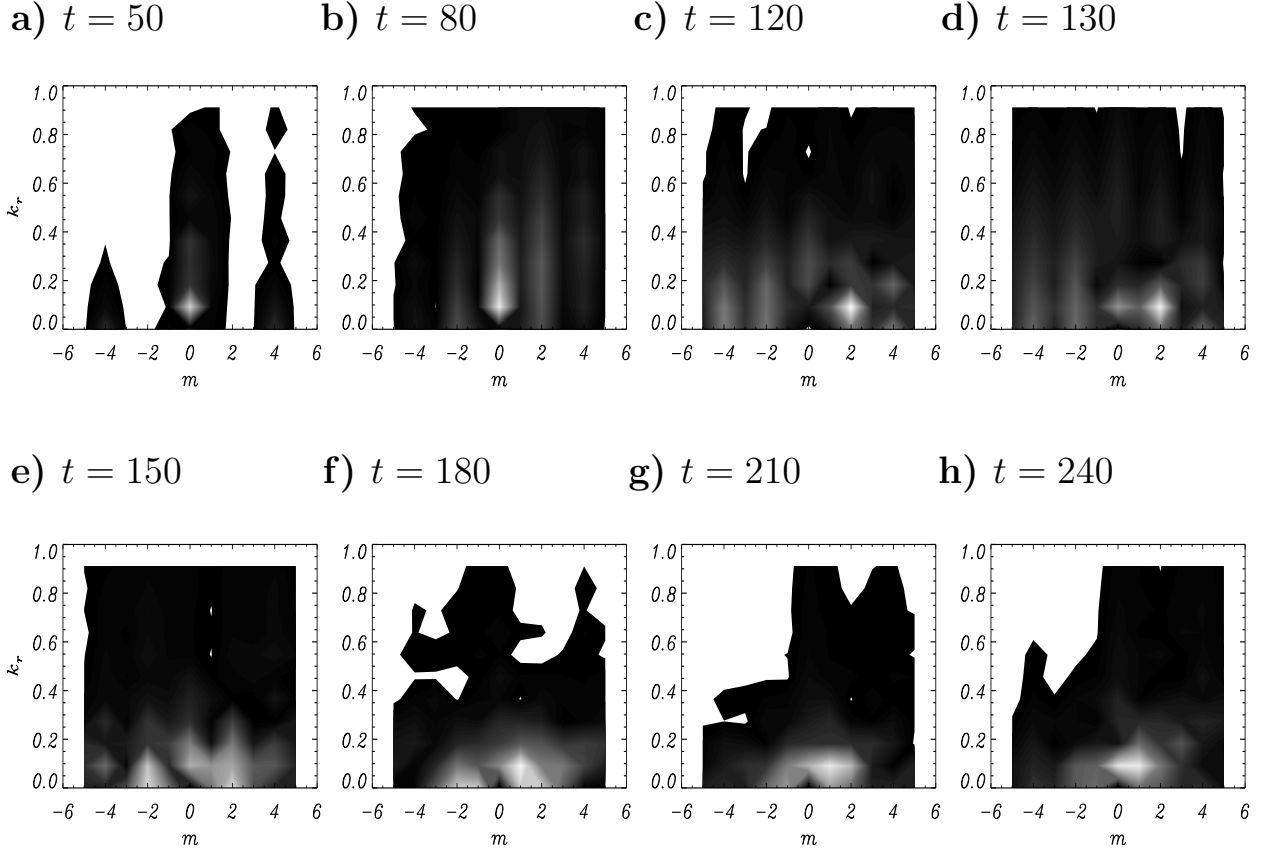


Fig. 18.— Amplitudes of modes with radial wave number (k_r) and azimuthal wave number (m) for the x - y pressure slice at $z = 25.0$ for simulation E shown at the same times as Fig. 11. The grey scale ranges from white (high amplitudes) to black (low amplitudes).

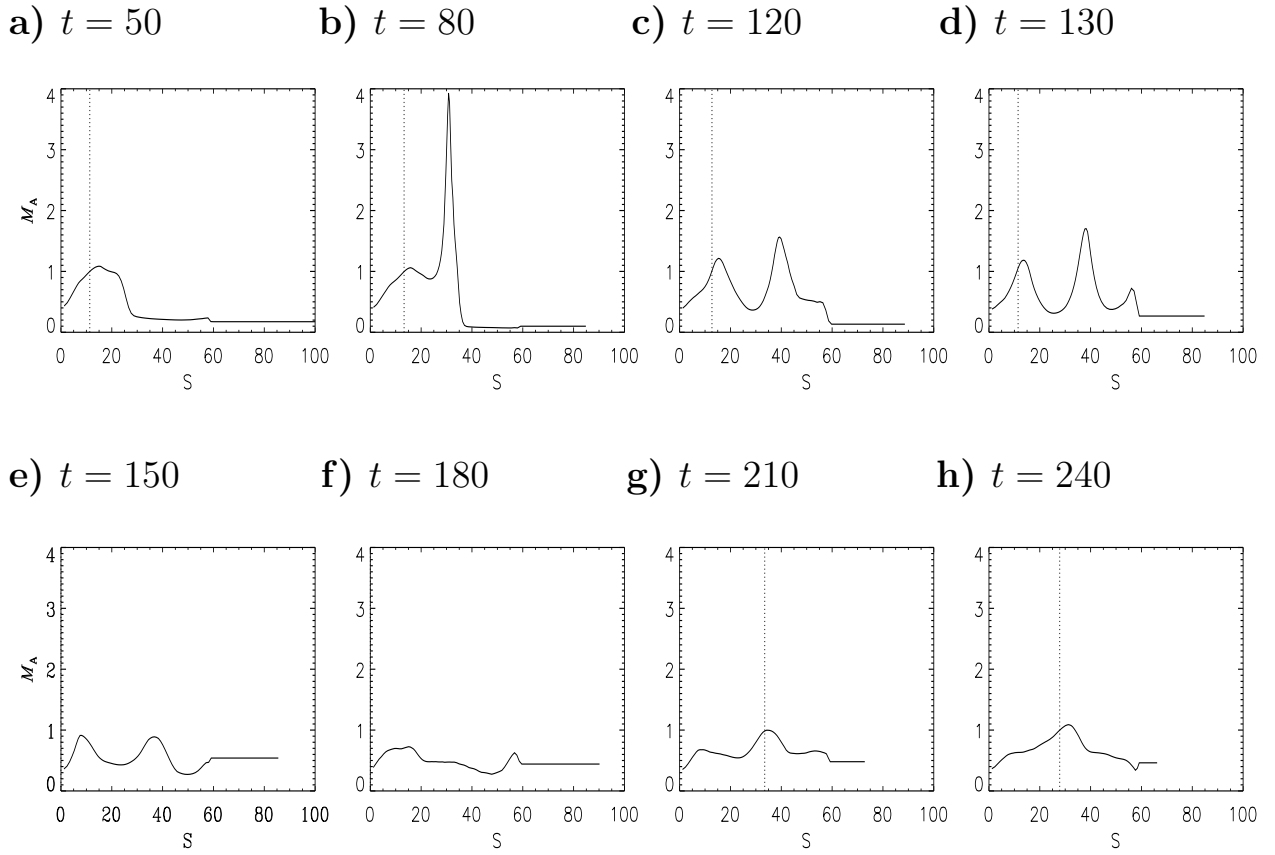
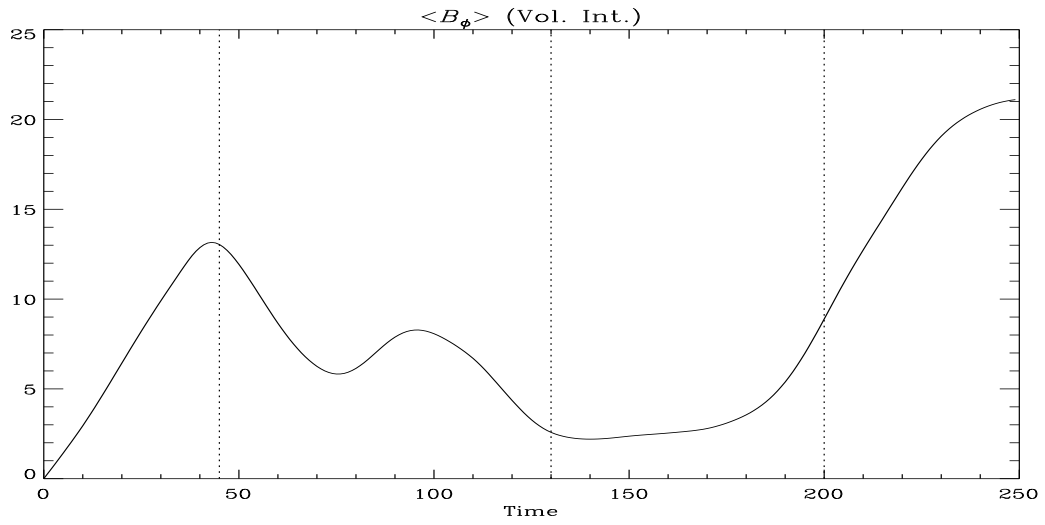


Fig. 19.— Alfvén Mach number (M_A) along the innermost magnetic field line of simulation E shown at the same times as Fig. 11. The s -axis is the distance along the field line (arc length). The vertical dashed lines mark the location, s_A , of the Alfvén point.

a)



b)

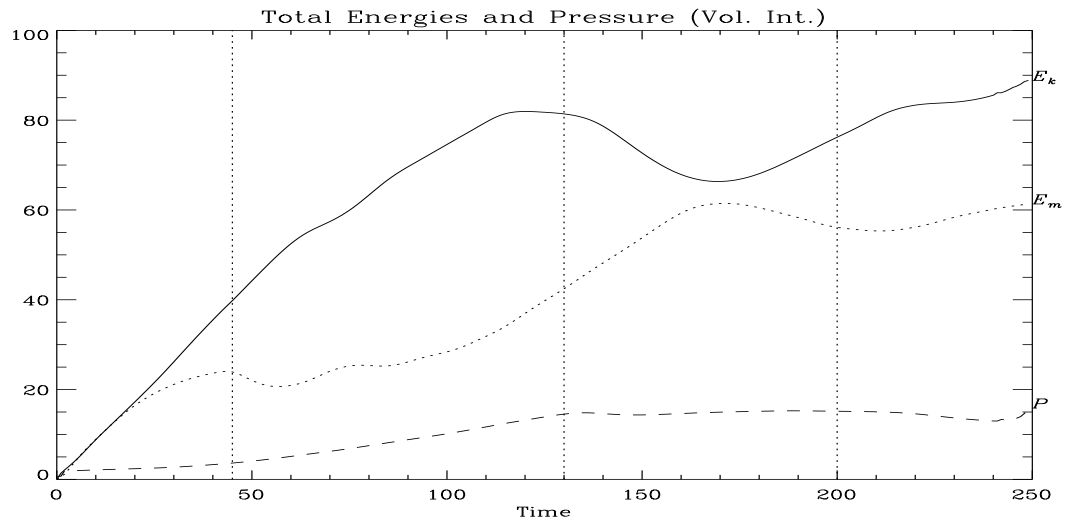


Fig. 20.— a) The time evolution of the mean toroidal magnetic field integrated over the primary computational domain of simulation E. b) The time evolution of the bulk magnetic (E_m), kinetic (E_k), and thermal (P) energies, integrated over the primary computational domain of simulation E.

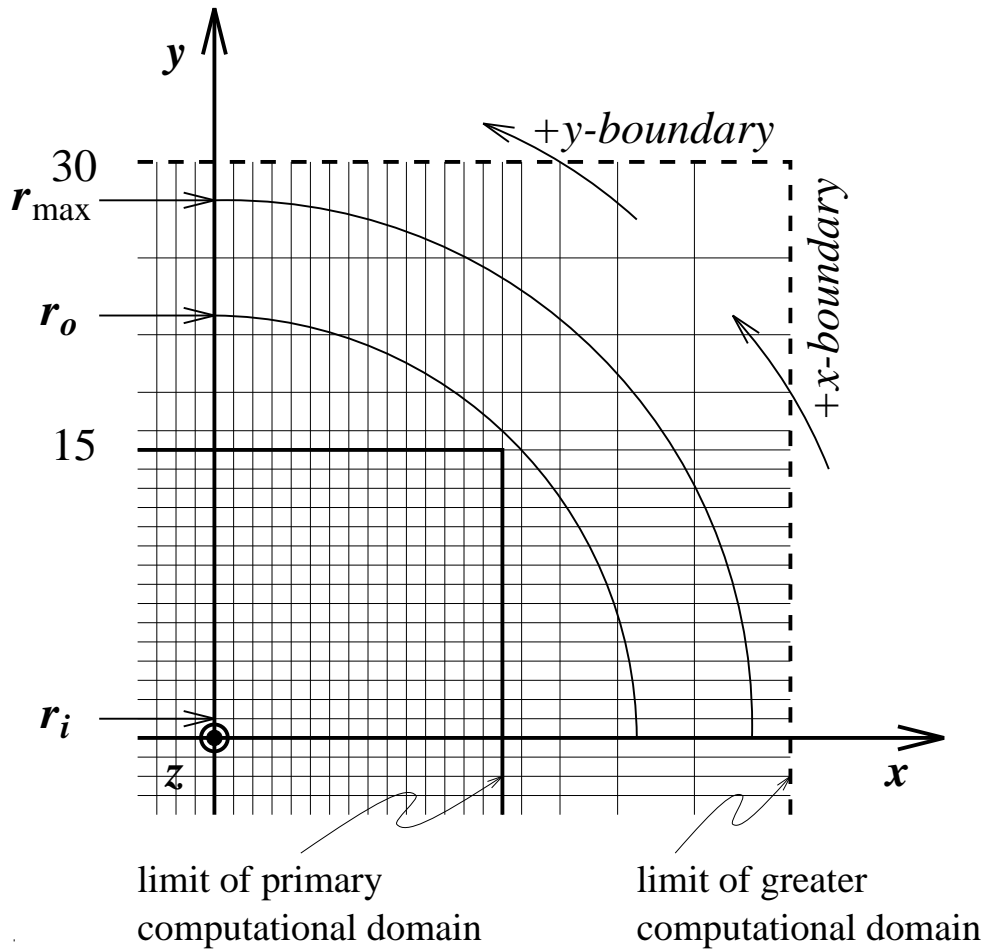


Fig. 21.— An x - y slice of the grid (for simulations A, B, C, and E) as viewed from above the $+z$ -axis. Rotation of the disc in the counter-clockwise direction would require material to flow in across the $+x$ -boundary, and then out again across the $+y$ -boundary. Since both boundaries are outflow, the first requirement is impossible. Thus, the Keplerian profile of the disc is reduced to zero smoothly between r_o and r_{\max} [equation (A.2)], preventing the corners from being evacuated. As in Fig. 1, only every second zone is indicated.

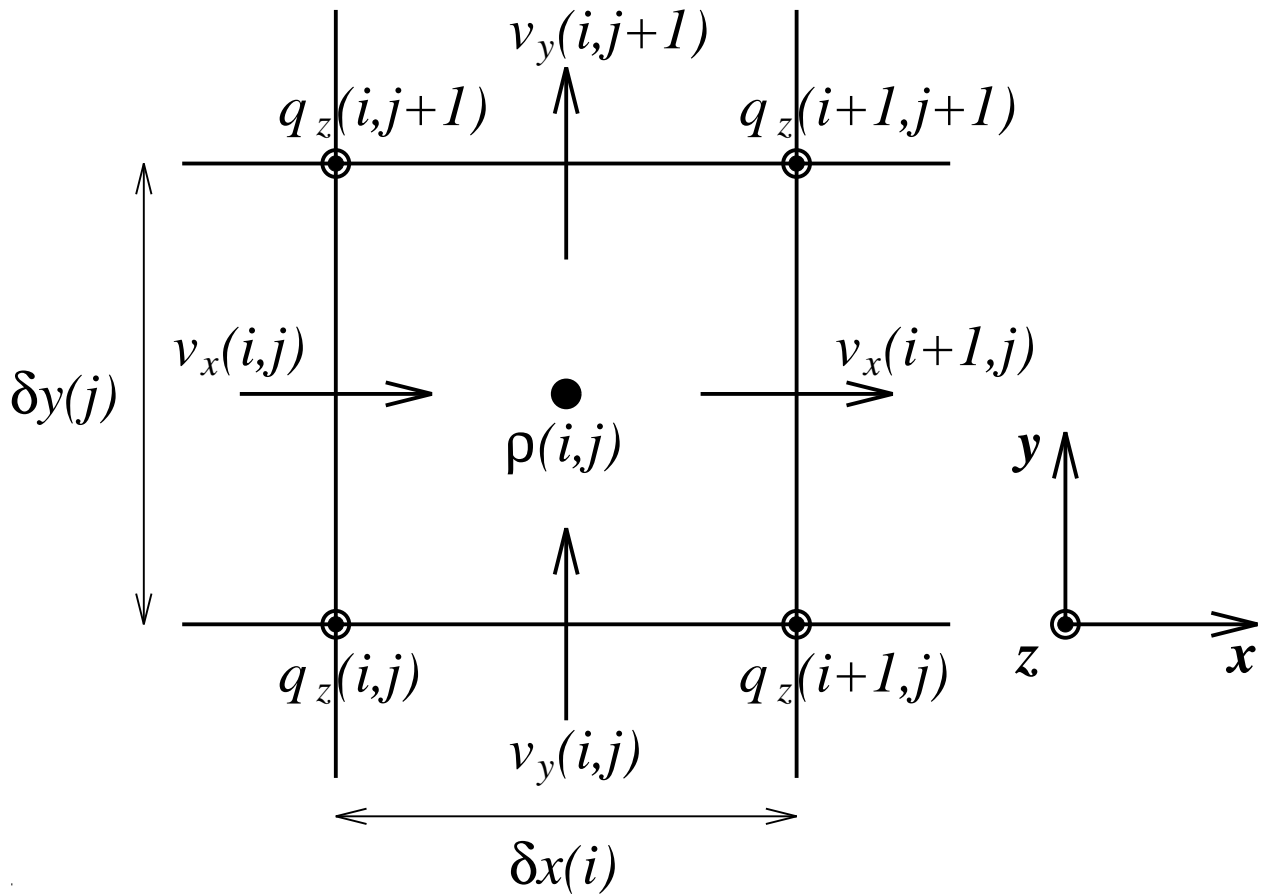


Fig. 22.— In the staggered mesh, variables are not all cospatial. In particular, scalars such as the density are located at the zone-centres, while primary vector components such as the velocity are face-centred as shown. Derived vector components, such as the “velocity vector potential” (q_z) are edge-centred.